Engineering the plant intracellular immune receptor Sr50 to restore recognition of the AvrSr50 escape mutant

Kyungyong Seong[1], Wei Wei[1], Brandon Vega[1], Amanda Dee[1], Griselda Ramirez-Bernardino[1], Rakesh Kumar[1], Lorena Parra[1] and Ksenia Krasileva[1,2,*]

[1] Department of Plant and Microbial Biology, University of California, Berkeley, CA 94720, USA.

[2] Innovative Genomics Institute, University of California, Berkeley, CA 94704

*To whom correspondence should be addressed: kseniak@berkeley.edu

Abstract

Sr50, an intracellular nucleotide-binding leucine-rich repeat receptor (NLR), confers resistance of wheat against stem rust caused by the fungal pathogen *Puccinia graminis* f. sp. *tritici*. The receptor recognizes the pathogen effector AvrSr50 through its C-terminal leucine-rich repeat domain, initiating a localized cell death immune response. However, this immunity is compromised by mutations in the effector, as in the escape mutant AvrSr50^{QCMJC}, which evades Sr50 detection. In this study, we employed iterative computational structural analyses and site-directed mutagenesis for rational engineering of Sr50 to gain recognition of AvrSr50^{QCMJC}. Following an initial structural hypothesis driven by molecular docking, we identified the Sr50^{K711D} single mutant, which induces an intermediate immune response against AvrSr50^{QCMJC} without losing recognition against AvrSr50. Increasing gene expression with a stronger promoter enabled the mutant to elicit a robust response, indicating weak effector recognition can be complemented by enhanced receptor expression. Further structural refinements led to the creation of five double mutants and two triple mutants with dual recognition of AvrSr50 and AvrSr50^{QCMJC} with greater immune response intensities than Sr50^{K711D} against the escape mutant. All effective mutations against AvrSr50^{QCMJC} required the K711D substitution, indicating that multiple solutions exist for gain of recognition, but the path to reach these mutations may be confined. Furthermore, this single substitution alters the prediction of AlphaFold 2, allowing it to model the complex structure of Sr50^{K711D} and AvrSr50 that match our final structural hypothesis. Collectively, our study outlines a framework for rational engineering of NLR systems to overcome pathogen escape mutations and provides datasets for future computational models for NLR resurrection.

Introduction

Plant intracellular immunity relies on nucleotide-binding leucine-rich repeat receptors (NLRs) that monitor and detect pathogen activities within cells (Jones and Dangl 2006). Upon direct recognition of pathogen effector molecules, NLRs trigger immune responses, typically culminating in localized cell death known as a hypersensitive response (HR) (Dodds and Rathjen 2010). The ability of NLRs to impede pathogen proliferation has driven researchers and breeders to identify functional NLRs and deploy them in genetic protection strategies for important crops (Dangl et al. 2013; Arora et al. 2019). Notably, Sr50, originally identified in rye, has been effectively utilized to protect wheat (*Triticum aestivum*) against stem rust disease caused by the fungal pathogen *Puccinia graminis* f. sp. *tritici* by directly recognizing its cognate effector AvrSr50 (Mago et al. 2015).

41   Pathogens counteract plant defenses through evolution of their effectors, enabling them to evade NLR-mediated
42   immune responses (Möller and Stukenbrock 2017; Sánchez-Vallet et al. 2018). For example, the *P. graminis* f. sp.
43   *tritici* isolate QCMJC secretes a variant of AvrSr50 (hereafter referred to as AvrSr50^{QCMJC}) that escapes Sr50
44   recognition with a single substitution, Q121K, on the protein surface (Chen et al. 2017; Ortiz et al. 2022). This escape
45   mutant compromises plant immunity and subsequently poses threats to genetically uniform crops. However, restoring
46   the effectiveness of NLRs remains a significant challenge, as the mutational landscape to be explored is extensive
47   (Tamborski and Krasileva 2020; Zdrzałek et al. 2023).

48   Key structural biology techniques, such as cryogenic electron microscopy (Cryo-EM) and crystallography, have been
49   instrumental in deciphering the complex binding mechanisms between NLRs and effectors, guiding subsequent
50   bioengineering efforts (Wang et al. 2019a, 2019b; Ma et al. 2020; Martin et al. 2020; Cesari et al. 2022; Förderer et
51   al. 2022; Zhao et al. 2022; Contreras et al. 2023; Liu et al. 2023; Maidment et al. 2023; Selvaraj et al. 2023; Kourelis
52   et al. 2024; Lawson et al. 2024; Madhuprakash et al. 2024). Yet, dependency on specialized expertise, experimental
53   challenges in protein purification and extensive resources limit applicability of crystallography and Cryo-EM
54   techniques to the full spectrum of NLR-effector pairs. Computational structure prediction has emerged as a potential
55   alternative to address this issue. AlphaFold 2 (AF2) and 3 (AF3) have been used to understand NLR oligomerization
56   and to elucidate the interaction between MLA3, an NLR from barely, and its effector Pwl2 (Evans et al. 2021; Jumper
57   et al. 2021; Abramson et al. 2024; Gómez De La Cruz et al. 2024, 2024; Madhuprakash et al. 2024). However, their
58   low accuracy was challenged by a recently solved Cryo-EM structure of MLA13 and its effector Avr$_{A13}$-1 (Lawson et
59   al. 2024). In such circumstances where molecular interactions between most NLRs and effectors cannot be fully
60   provided, engineering NLRs requires development of new rational engineering approaches that can be successful with
61   incomplete information.

62   Despite the inherent difficulties, significant strides have been made in NLR engineering. Advancements include
63   engineering small integrated domains (IDs) found in a subset of NLRs as platforms for effector binding (Kroj et al.
64   2016; Sarris et al. 2016; Baggs et al. 2017). Particularly, rational design strategies focusing on heavy-metal associated
65   domains (HMAs), guided by crystallography structures, have shown promise by altering or transferring effector
66   recognition specificity (De La Concepcion et al. 2019; Cesari et al. 2022; Bentham et al. 2023; Maidment et al. 2023).
67   Conversely, engineering the C-terminal leucine-rich repeat (LRR) domain, postulated to participate in effector binding
68   across most NLRs, remains a challenging pursuit. Most studies resort to gain-of-function random mutagenesis to
69   counter escape effector mutants (Farnham and Baulcombe 2006; Harris et al. 2013; Segretin et al. 2014; Huang et al.
70   2021). In our recent endeavor, we harnessed the natural sequence diversity of NLRs, pinpointing and targeting rapidly
71   evolving, highly variable (hv) residues to switch recognition specificity between two related NLRs (Prigozhin and
72   Krasileva 2021; Tamborski et al. 2023). Nevertheless, receptor-centric random mutagenesis and engineering
73   approaches do not consider how the effectors are bound to the receptors and overlook the residual interplay between
74   them. When effectors mutate, therefore, numerous receptor residues need to be re-screened to resurrect the NLRs.
75   Consequently, there is a pressing need for methodologies that can illuminate the conformation of NLR and effector as
76   a part of the rational LRR design.

77   In this study, we engineer Sr50 to recognize the escape mutant AvrSr50^{QCMJC}. We employ a strategic combination of
78   site-directed mutagenesis, molecular docking and structural analyses to iteratively infer and refine the heterodimeric
79   structure of Sr50 and AvrSr50. Guided by predictive models through molecular docking simulations, we introduced
80   mutations to charged or polar residues of Sr50 and AvrSr50, which likely govern ligand-receptor specificity, to disrupt
81   effector recognition or mediate recognition escape, respectively (Fig. 1A). We then tested their complementary
82   AvrSr50 and Sr50 mutants in *Nicotiana benthamiana* to experimentally corroborate residual proximity and leveraged
83   it to refine our structural hypotheses with ColabDock (Feng et al. 2023). In this iterative process, we generated single,
84   double, and triple mutants of Sr50 that induced variable levels of cell death against AvrSr50^{QCMJC}. Interestingly, all

85 successful mutation combinations required the K711D substitution to result in gain of AvrSr50^{QCMJC} recognition.
86 Furthermore, although AF2-Multimer could not predict the structure of Sr50 and AvrSr50, it could model the complex
87 structure of Sr50^{K711D} bound to AvrSr50 and AvrSr50^{QCMJC}. This predicted AF2 model showed good agreement with
88 our final structural hypothesis, indicating that the outcomes from different approaches converged. Collectively, our
89 exploration extended beyond engineering solutions, providing not only valuable insights of the Sr50 and AvrSr50
90 interaction, but also training datasets and rational design strategies that can be expanded to other systems.
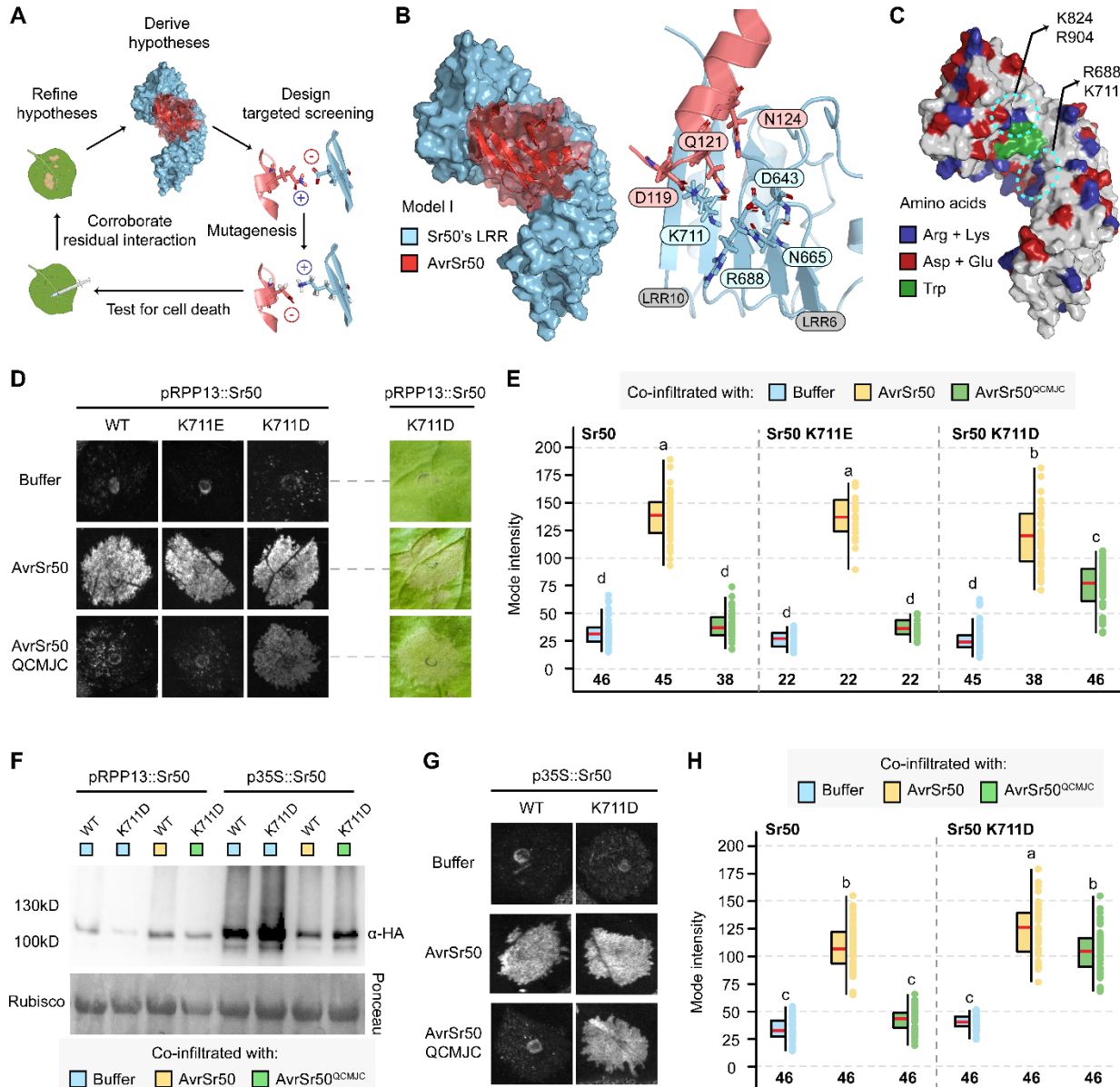
Figure 1. Initial structural hypotheses derived from molecular docking simulations and gain of AvrSr50^{QCMJC} recognition

A. A generalized workflow of structure-guided NLR engineering. **B.** A predicted pose of Sr50 and AvrSr50 by molecular docking simulations. Some parts of a loop between β2–β3, mostly including an unstructured region, are removed from AvrSr50 for visualization (positions 42-66). The local environment around AvrSr50's Q121 is visualized. **C**. The distribution of selected amino acids across the surface of Sr50's leucine-rich repeat (LRR) domain. **D** and **E**. The qualitative and quantitative cell death phenotypes

98 on *Nicotiana benthamiana*. The optical density (OD_{600}) was set to 0.3 for receptors and effectors, respectively, and the receptors
99 were expressed under pRPP13. Indicated receptor and effector pairs were co-infiltrated. The cell death phenotypes were recorded
100 at three days post infiltration (dpi). **E**. The mode intensity of the infiltrated spots was measured with imageJ across the given number
101 of biological replicates in bold. The statistics were calculated with one-way ANOVA followed by a post-hoc Tukey HSD (Honestly
102 Significant Difference) test. The compact letters indicate significant differences between groups. **F**. Representative Western blot
103 for the wild type Sr50 and the Sr50^{K711D} mutant under pRPP13 or p35S. **G** and **H**. The qualitative and quantitative cell death
104 phenotypes on *N. benthamiana*. The OD_{600} was set to 0.1 for receptors and 0.3 for effectors, respectively, and the receptors were
105 expressed under p35S. The cell death phenotypes were recorded at 2 dpi. **H**. The mode intensity of the infiltrated spots was
106 measured with imageJ across the given number of biological replicates in bold. The statistics were calculated with one-way
107 ANOVA followed by a post-hoc Tukey HSD test.

Results

Initial structural hypothesis generation with molecular docking

110 To formulate our initial structural hypothesis, we attempted modeling the heterodimeric complex of Sr50 and AvrSr50
111 with AF2-Multimer and AF3. However, the reported accuracy was low, indicating uncertainty in the prediction (Fig.
112 S1). We alternatively turned to molecular docking algorithms to generate a set of initial structural hypotheses based
113 on specific criteria drawn from the Sr35 resistosome structure and the assumption that AvrSr50's Q121K directly
114 participates in binding through its interaction with Sr50's LRR residues (Förderer et al. 2022; Ortiz et al. 2022; Zhao
115 et al. 2022). Our intention was to diversify the initial hypotheses and gather more experimental data to either support
116 or disprove these models (Fig. 1A).

117 The molecular docking simulations produced three distinct models (Fig. 1B; Fig. S2). We prioritized two of these
118 poses that aligned with our simplified assumption: the Q121K substitution in AvrSr50^{QCMJC} results in repulsive
119 interactions with an amino acid side chain in Sr50, which impedes effector recognition. In the first model (Fig. 1B),
120 AvrSr50's Q121 was proximal to two positively charged residues of Sr50, R688 on LRR 8 and K711 on LRR 9. An
121 alternative model (Fig. S2A) positioned Q121 in the vicinity of K824 on LRR 13 and R904 on LRR 16. These four
122 charged residues form a neighboring cluster of tryptophan residues across LRRs 11 to 13, which might offer affinity
123 for effector binding (Fig. 1C). We hypothesized that the two selected regions may determine specificity for AvrSr50,
124 and modifying one of these two interfaces could recover the interaction with AvrSr50^{QCMJC}.

Sr50^{K711D} induces cell death against AvrSr50^{QCMJC} without losing the interaction with AvrSr50

126 To test the initial hypotheses about incompatible side chain interactions between Sr50 and AvrSr50^{QCMJC}, we
127 introduced aspartic and glutamic acid into R688, K711, K824 and R904 of Sr50. These specific substitutions were
128 selected based on our simplified assumption to re-establish complementary interactions with Q121K of AvrSr50^{QCMJC}
129 through ionic or hydrogen bonds. Subsequently, we infiltrated *N. benthamiana* with *Agrobacterium* carrying Sr50
130 single mutants and AvrSr50 or AvrSr50^{QCMJC}. The expression of the receptors was driven by a native promoter of
131 NLR RPP13 to avoid autoactivity (Tamborski et al. 2023). The aspartic and glutamic acid substitutions at K824 and
132 R904 led to the loss of HR against AvrSr50; however, none of these receptor mutants could mediate AvrSr50^{QCMJC}-
133 dependent cell death (Fig. S3). The mutations on Sr50's R688 neither completely abolished HR against AvrSr50 nor
134 led to the gain of AvrSr50^{QCMJC} recognition (Fig. S3). Sr50^{K711D} and Sr50^{K711E} did not compromise the receptor's
135 ability to recognize AvrSr50 (Fig. 1D and 1E). While Sr50^{K711E} could not restore HR against AvrSr50^{QCMJC}, Sr50^{K711D}
136 induced AvrSr50^{QCMJC}-dependent cell death. Compared to Sr50 and AvrSr50, the restored HR was weaker in intensity,
137 likely indicating suboptimal interactions of Sr50^{K711D} towards AvrSr50^{QCMJC}. Nonetheless, these experiments
138 suggested that Sr50^{K711D} gained recognition against AvrSr50^{QCMJC} without losing the interaction with AvrSr50.

Weak recognition of Sr50^{K711D} can be complemented by strong gene expression

To determine whether the increased HR of Sr50^{K711D} in response to AvrSr50^{QCMJC} was due to difference in protein abundance, we estimated relative quantity of Sr50 and Sr50^{K711D} following their co-infiltration with AvrSr50 and AvrSr50^{QCMJC}, respectively, using Western blot (Fig. 1F). Unexpectedly, we consistently observed lower protein levels of Sr50^{K711D} compared to Sr50 under the RPP13 promoter. We postulated that assessment of the magnitude of cell deaths may be confounded by the difference in protein abundance. To drive receptor abundance to comparable levels, we instead used the constitutive 35S promoter from the Cauliflower Mosaic Virus.

Under the 35S promoter, the protein level of Sr50^{K711D} was slightly greater than Sr50 after co-infiltrations with AvrSr50^{QCMJC} and AvrSr50, respectively (Fig. 1F). In consistency, the average mode intensity of HR appeared higher for p35S::Sr50^{K711D} than p35S::Sr50 at two days post-infiltration , when the receptors were co-infiltrated with AvrSr50 (Fig. 1G and 1H). Notably, the HR induced by p35S::Sr50^{K711D} and AvrSr50^{QCMJC} was similar in magnitude to p35S::Sr50 and AvrSr50 (Fig. 1G and 1H). This suggested that the Sr50^{K711D} mutant does recognize AvrSr50^{QCMJC} and that potentially weak recognition of Sr50^{K711D} was complemented by strong expression driven by the 35S promoter for enhanced immune responses. Although altering the promoter is a viable engineering strategy, we continued our pursuit with the weaker RPP13 promoter to further enhance the recognition of Sr50^{K711D} through additional amino acid mutations.

Sr50^{K711D} does not recognize the AvrSr50^{Q121K} single mutant

To generate Sr50 mutants capable of inducing robust HR against AvrSr50^{QCMJC} under the RPP13 promoter, we aimed to refine our structural model to better guide targeted mutagenesis. The observed gain of function in Sr50^{K711D} was not direct confirmation of the existing structural hypothesis (Fig. 1B). The mature forms of AvrSr50 and AvrSr50^{QCMJC} have ten substitutions, including the Q121K substitution which has been shown to mediate recognition escape (Fig. 2A; Fig. S4) (Ortiz et al. 2022). It was therefore crucial to determine whether Sr50^{K711D} could induce HR against the AvrSr50^{Q121K} single mutant. As reported previously (Ortiz et al. 2022), reverting K121 of AvrSr50^{QCMJC} to glutamine as in AvrSr50 was sufficient to restore the HR for Sr50 and Sr50^{K711D} (Fig. 2B and 2C) However, co-infiltration of Sr50^{K711D} and AvrSr50^{Q121K} did not lead to cell death. This possibly suggested that the interaction between Sr50's K711D and AvrSr50's Q121K may not be one-to-one, and there might be other effector and receptor residues involved in interaction.

Mutations in AvrSr50's N124 alter the interaction with Sr50 but may not be associated with Sr50's K711

The lack of HR between Sr50^{K711D} and AvrSr50^{Q121K} prompted a reassessment of other factors potentially influencing the interaction. Notably, AvrSr50^{QCMJC} carries another adjacent substitution, N124T, along the terminal alpha helix (Fig. 2A). We postulated that this adjacent mutation might contribute to the differential responses of Sr50^{K711D} towards AvrSr50^{QCMJC} and AvrSr50^{Q121K}.

Additional experiments with the AvrSr50^{N124T} single mutant revealed that this substitution alone did not significantly impact the interaction with Sr50 and Sr50^{K711D} (Fig. 2B and 2C). However, co-infiltration of Sr50^{K711D} and the AvrSr50$^{Q121K/N124T}$ double mutant partially restored the cell death phenotype. Consistently, the presence of N124 in AvrSr50$^{QCMJC\ K121Q}$ tended to attenuate the intensity of HR, compared to the AvrSr50$^{QCMJC\ K121Q}$ single mutant. This suggested that the amino acid variations at position 124 of AvrSr50 alter the interaction with the receptor.
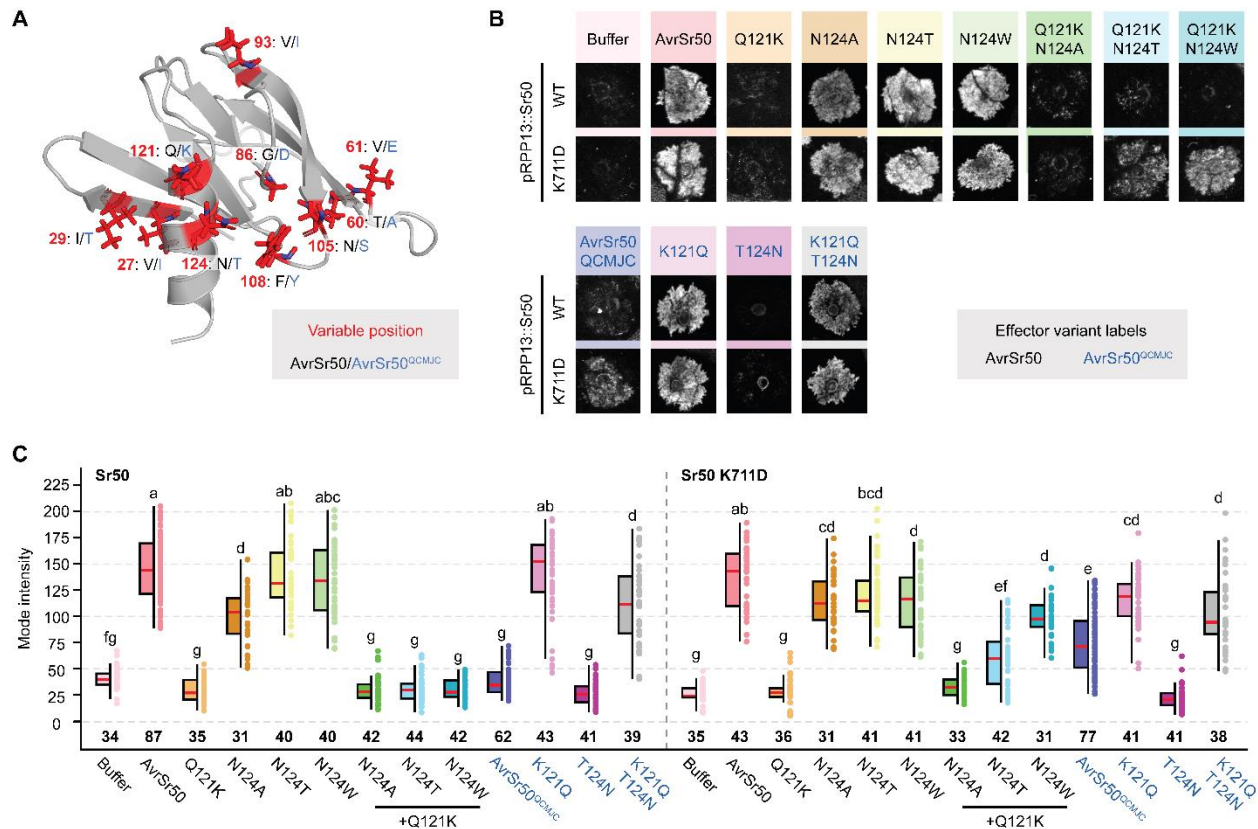
**Figure 2. Mutations in AvrSr50's Q121 and N124 alter the interaction with Sr50**

A. Variable positions between AvrSr50 and AvrSr50^{QCMJC}. Amino acid variations between the two proteins are indicated in the predicted structure of AvrSr50 without its mature form. **B** and **C**. The qualitative and quantitative cell death phenotypes on *Nicotiana benthamiana*. The optical density (OD$_{600}$) was set to 0.3 for receptors and effectors, respectively, and the receptors were expressed under pRPP13. Indicated receptor and effector pairs were co-infiltrated. The cell death phenotypes were recorded at three days post infiltration. **B**. The mode intensity of the infiltrated spots was measured with imageJ across the given number of biological replicates in bold. The statistics were calculated with one-way ANOVA followed by a post-hoc Tukey Honestly Significant Difference test. The compact letters indicate significant differences between groups.

To gain further mechanistic insights, we substituted AvrSr50's N124 to two very distinct amino acids, alanine and tryptophan. Unexpectedly, the AvrSr50$^{Q121K/N124W}$ double mutant increased HR when co-infiltrated with Sr50^{K711D}, compared to AvrSr50^{Q121K}. Yet, this enhanced HR was also observed in the co-infiltration with Sr50^{K711A} and Sr50^{K711E} (Fig. S5). This likely indicated that AvrSr50's N124 may not form specific interactions with Sr50's K711D and may be simply located in an environment that favors a bulky hydrophobic amino acid. In accordance with this postulation, AvrSr50^{N124A} diminished cell death, and AvrSr50$^{Q121K/N124A}$ failed to enhance HR (Fig. 2B and 2C). The phenotypic changes mediated by AvrSr50 N124 mutants without specific association with the K711D substitution suggested that while AvrSr50's Q121K and N124T contact the LRR domain of Sr50, they may not be interacting with Sr50's K711D.

Sr50's K824 and R904 form an additional contact with AvrSr50

To improve our structural model, we decided to explore another possible contact point between the receptor and the effector from the initial structural hypothesis (Fig. 1A and 1B). Our previous experiments supported that the upper part of AvrSr50's terminal alpha helix is involved in the interaction with Sr50 (Fig. 2). Additionally, our initial

197 screening showed that mutating K824 or R904 in Sr50 to negatively charged amino acids resulted in the complete or
198 near loss of AvrSr50 recognition (Fig. S3). We hypothesized that Sr50's K824 and R904 interact with negatively
199 charged side chains of AvrSr50.
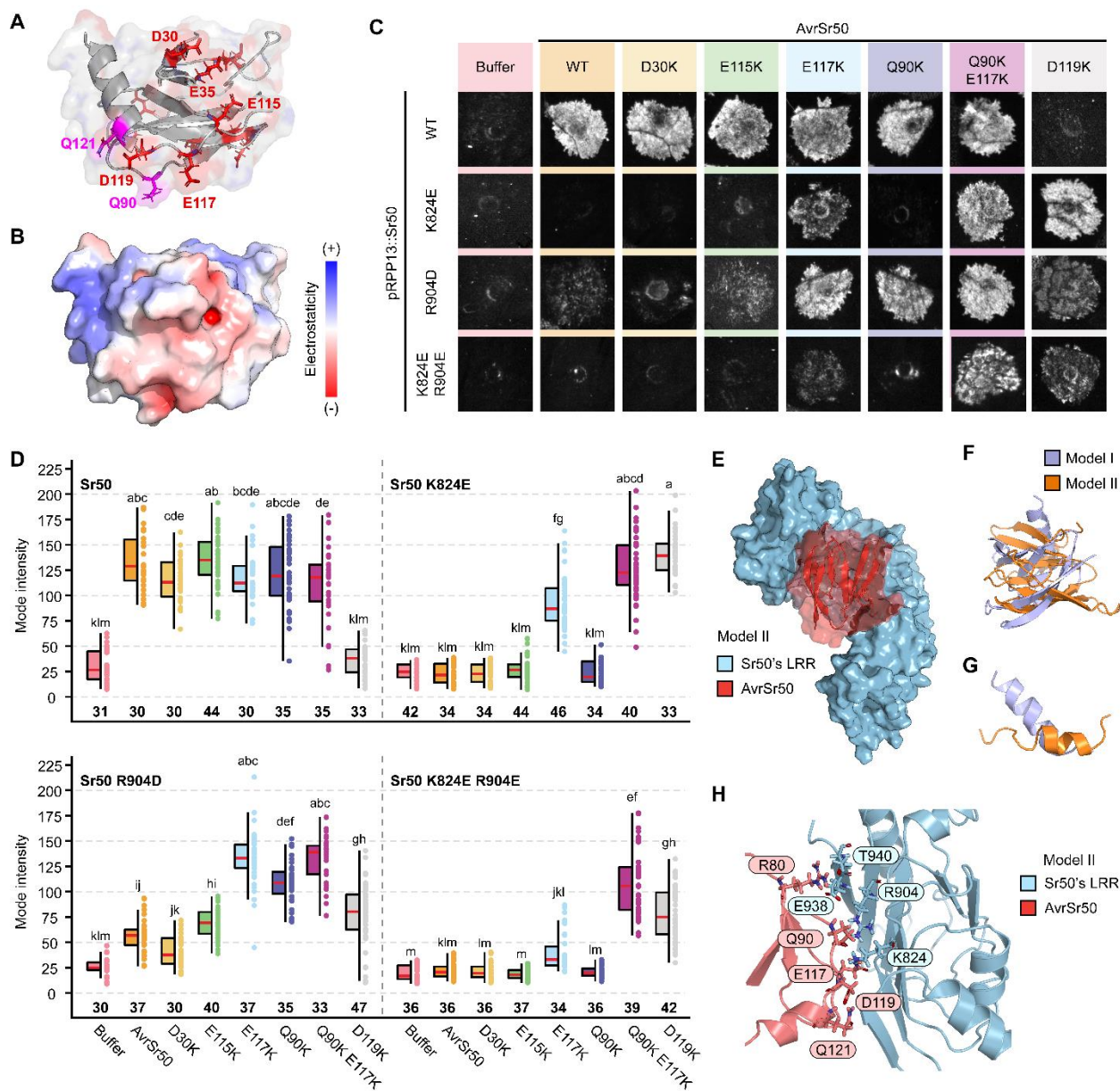
200
201 **Figure 3. Sr50's K824 and R904 in terminal leucine-rich repeats form a critical effector binding interface**

202 **A** and **B.** The predicted structure of AvrSr50. The orientation of the structure is identical in both panels. **A.** Negatively charged
203 amino acids are indicated in red, as well as Q90 and Q121 in purple. **B.** The estimated electrostatic potential is mapped to the
204 surface of AvrSr50. **C** and **D.** The qualitative and quantitative cell death phenotypes on *Nicotiana benthamiana*. The optical density
205 (OD_{600}) was set to 0.3 for receptors and effectors, respectively, and the receptors were expressed under pRPP13. Indicated receptor
206 and effector pairs were co-infiltrated. The cell death phenotypes were recorded at three days post infiltration. **D.** The mode intensity
207 of the infiltrated spots was measured with imageJ across the given number of biological replicates in bold. The statistics were
208 calculated with one-way ANOVA followed by a post-hoc Tukey Honestly Significant Difference test. The compact letters indicate

209   significant differences between groups. **E**. The predicted poses of Sr50 and AvrSr50 in Model II. Some parts of a loop between
210   β2–β3, mostly including an unstructured region, are removed from AvrSr50 for visualization (positions 42-66). **F** and **G**. The
211   superposition of AvrSr50 in Model I and II. The entire complex structures of the two models were superposed to fix the coordinates
212   of Sr50 consistent. The AvrSr50 structures are then visualized. **G**. Only the terminal alpha helix of AvrSr50 is displayed from the
213   superposed AvrSr50 structures. **H**. The local environment around Sr50's K824 and R904 in Model II.

214   Positioning AvrSr50's alpha helix adjacent to the LRR domain of Sr50 as in the initial structural hypothesis (Fig. 1B)
215   and mapping the locations of negatively charged amino acids (Fig. 3A), we identified two aspartic acids and three
216   glutamic acids that create a surface with negative electrostatic potential and may face the LRR domain (Fig. 3B).
217   Under the postulation that some of these residues could restore interactions with $Sr50^{K824E}$ and $Sr50^{R904D}$, we mutated
218   each of these residues to lysine. Two exceptions were AvrSr50's E35, which is internally bound to K28 and K79
219   possibly for protein stability (Fig. S6), and D119 closely located to Q121 and unlikely to contact the two receptor
220   residues in our current hypothesis (Fig. 1B).

221   Consequently, we created $AvrSr50^{D30K}$, $AvrSr50^{E115K}$ and $AvrSr50^{E117K}$ and co-infiltrated them with $Sr50^{K824E}$ or
222    $Sr50^{R904D}$ (Fig. 3C and 3D). $AvrSr50^{D30K}$ neither disrupted the interaction with Sr50 nor restored the cell death
223   phenotypes of the Sr50 mutants. $AvrSr50^{E115K}$ induced some HR against $Sr50^{R904D}$, the magnitude of which is slightly
224   higher than $Sr50^{R904D}$ and AvrSr50. Notably, $AvrSr50^{E117K}$ induced strong cell death against both $Sr50^{K824E}$ and
225    $Sr50^{R904D}$. This suggested that AvrSr50's E117 is possibly proximal to Sr50's K824 and R904.

226   **Refining structural hypotheses with experimental constraints**

227   The identification of the contact point between Sr50's K824 and R904 and AvrSr50's E117 enabled updating our
228   structural hypothesis (Fig. 1A). We used ColabDock to constrain four pairs of residues from Sr50 and AvrSr50 and
229   infer a new structural model. Two pairs—K824 and E117, as well as R904 and E117—were derived from the
230   experimental data (Fig. 3C and 3D), and the other pairs—K711 and Q121, as well as K711 and N124—originated
231   from Model I, as we could not completely reject the initial structural hypothesis (Fig. 1B).

232   Our refined structural hypothesis, Model II, displayed notable changes in the position of AvrSr50 compared to Model
233   I (Fig. 3E and 3F). In this model, ColabDock distorted the structure of AvrSr50's terminal alpha helix to accommodate
234   the specified restraints (Fig. 3G). Inspecting the structure closely, we found that it would be impossible to physically
235   satisfy the constraints: the distance between AvrSr50's E117 and Q121 (Fig. 3A) is much smaller than the distance
236   between Sr50's K711 and K824 (Fig. 1C). This possibly suggested that not all the constraints driven from Model I are
237   correct, as our experiments hinted (Fig. 2). Sr50's K711 may indeed interact with some other residues than AvrSr50's
238   Q121 and N124, provided that the interaction between Sr50's K824 and R904 and AvrSr50's E117 was much more
239   plausible (Fig. 3C). Simulating molecular docking without the two constraints from Model I placed AvrSr50 at the
240   edge of the upper loop of LRRs (Fig. S7). This violated our experimental observations that suggest the involvement
241   of Sr50's K711 in the interactions (Fig. 1 and 2) and potentially indicated that ColabDock did not have algorithmic
242   power to predict the correct conformation without enough restraints. We therefore proceeded with Model II as our
243   next structural hypothesis.

244   **Additional AvrSr50 residues contact Sr50's K824 and R904**

245   As the structure of AvrSr50 became repositioned in Model II, additional charged or polar effector residues could
246   potentially interact with $Sr50^{K824E}$ and $Sr50^{R904D}$: Q90 and D119 (Fig. 3H). Unlike Model I, AvrSr50' D119 lied much
247   closer to these receptor residues. We evaluated the involvement of the two effector residues in interactions by co-
248   infiltrating $AvrSr50^{Q90K}$ and $AvrSr50^{D119K}$ with $Sr50^{K824E}$ and $Sr50^{R904D}$. $AvrSr50^{Q90K}$ could induce cell death against

249 Sr50^{R904D} but not Sr50^{K824E} (Fig. 3C and 3D). Furthermore, AvrSr50$^{Q90K/E117K}$ double mutant triggered robust HR
250 against the Sr50$^{K824E/R904E}$ double mutant, a response not observed with any of the single effector mutants. This
251 supported the AvrSr50's Q90 would interact with Sr50's R904. Similarly, AvrSr50^{D119K} could strongly restore the
252 abolished HR of Sr50^{K824E} and induced relatively weaker HR against Sr50^{R904D} and Sr50$^{K824E/R904E}$. Notably,
253 AvrSr50^{D119K} was the only effector mutant that abolished the interaction with Sr50 among the tested mutants at this
254 interface. This potentially suggested that AvrSr50's D119 may be critical for recognition, interacting with Sr50's
255 K824 and positioned closely to R904.

256 **Positively charged residues on the terminal LRR leads to auto-activity**

257 Following the revised hypothesis (Fig. 3H), we aimed to validate additional interaction between another pair of
258 residues: Sr50's E938 and AvrSr50's R80. However, Sr50^{E938K} showed strong auto-activity, making it challenging to
259 discern phenotypic changes upon co-infiltration with effector mutants (Fig. S8). Subsequently, we attempted Sr50^{T940K}
260 and Sr50^{T940R} mutants, but they also triggered severe auto-activity (Fig. S8). These outcomes potentially suggested
261 that the very terminal LRR unit might play a role in stabilizing inactive Sr50, and the introduction of positively charged
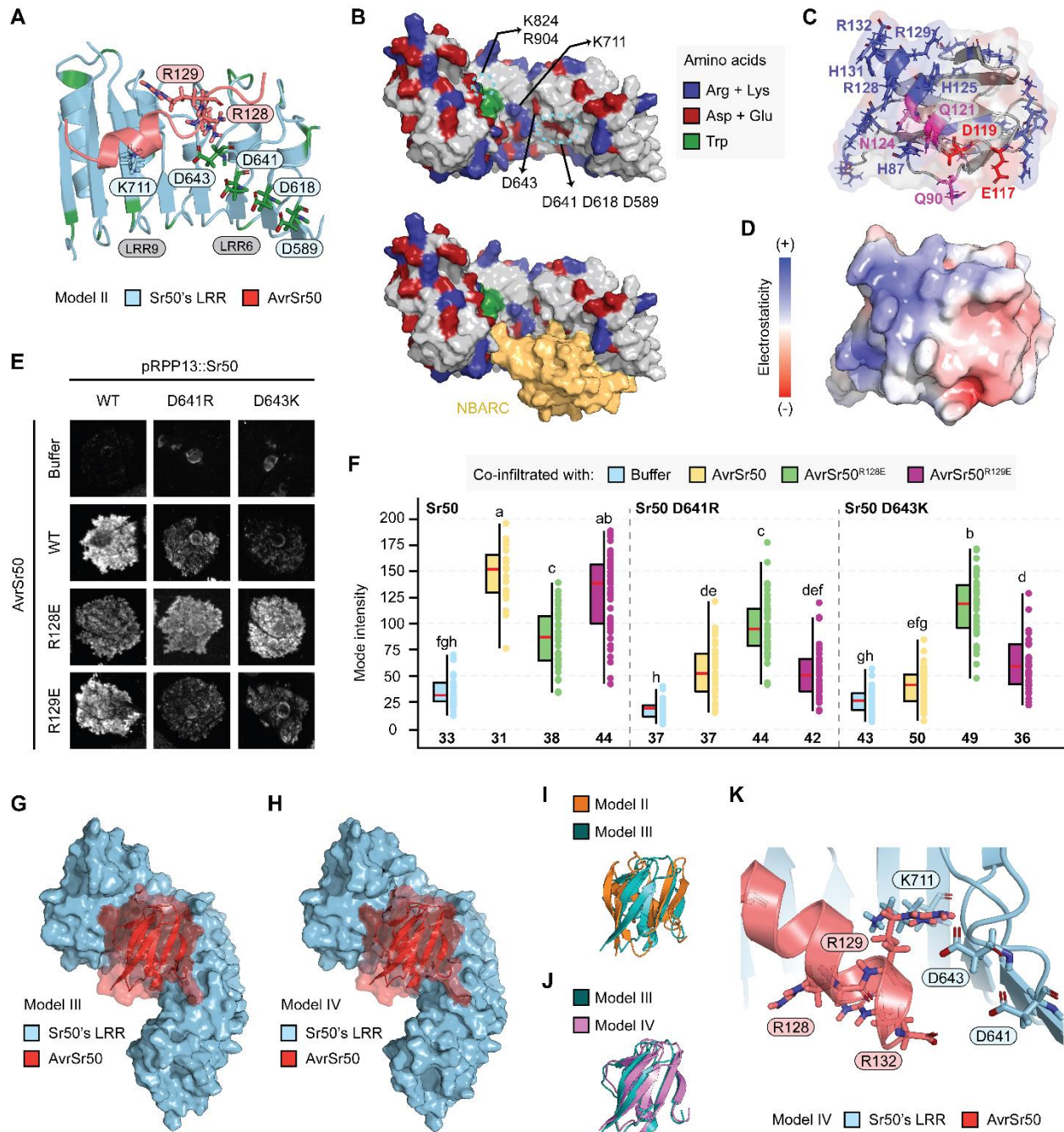262 residues in these positions might interfere with Sr50's stability.

263 **AvrSr50's alpha helix enriched with positively charged residues are positioned towards the inner concave of**
264 **the LRR domain**

265 Model II led to the identification of interacting receptor and effector residues. However, it was not a plausible
266 biological model with structural distortion (Fig. 3G). Some effector side chains, such as R128, were clashing into the
267 receptor backbones, creating physically impossible conformation (Fig. 4A). Nevertheless, we noted potential
268 electrostatic complementarity in this region. Near Sr50's K711 are negatively charged amino acids, D589, D618,
269 D641 and D643 (Fig. 4A and 4B). Although some of these residues, such as D589 and D618, contact the NB-ARC
270 domain potentially for interdomain stabilization and may not be available, the others could participate in the interaction
271 with the effector (Fig. 4B). Notably, AvrSr50 contains H125, R128, R129, H131 and R132 at the end of the terminal
272 alpha helix (Fig. 4C), which creates strong positive electrostatic potential (Fig. 4D) and potentially lies around the
273 negatively charged amino acids of Sr50 (Fig. 4A). In particular, R128 lies on the same plane as E117, D119, Q121
274 and N124 shown to alter the interaction with Sr50 mutants (Fig. 4C).

275 Based on these observations, we postulated that AvrSr50's R128 would interact with negatively charged amino acids
276 of Sr50, potentially D641 and D643 that are adjacent (Fig. 4A). We created AvrSr50^{R128E} and AvrSr50^{R129E} for
277 comparison and co-infiltrated them with Sr50^{D641R} or Sr50^{D643K}. Co-infiltration of Sr50^{D641R} or Sr50^{D643K} with AvrSr50
278 indicated that the mutations at these positions attenuate AvrSr50 recognition (Fig. 4E and 4F). AvrSr50^{R128E} generated
279 a variable phenotype from no cell death to strong HR in co-infiltration with Sr50. Nevertheless, AvrSr50^{R128E} could
280 clearly restore cell death for the Sr50^{D643K} mutant and increase the level of HR against the Sr50^{D641R} mutant. This
281 suggested that AvrSr50's R128 is possibly proximal to Sr50's D643, as indicated in our model.

282 **Refining structural hypotheses with experimental constraints and AlphaFold**

283 The collection of potential interacting receptor-effector residues was used as restraints to update our structural
284 hypothesis (Fig. 1A). These included D643 and R128, K824 and E117 as well as D119, and R904 and Q90, E117 as
285 well as D119 (Fig. 3 and 4). Compared to Model II, Model III slightly repositioned the AvrSr50 structure (Fig. 4G
286 and 4I), better fitting the terminal alpha helix of AvrSr50 into the groove of the LRR domain.

Figure 4. AvrSr50's alpha helix enriched with positively charged residues are positioned towards the inner concave of the LRR domain

A. The local environment around Sr50's K711 in Model II. Colored in green are aspartic and glutamic acids. **B**. The distribution of selected amino acids across the surface of Sr50's leucine-rich repeat (LRR) domain. In bottom, a portion of the NB-ARC domain that contacts LRR is included. **C** and **D.** The predicted structure of AvrSr50. The orientation of the structure is identical in both panels. **C**. Positively charged amino acids are indicated in blue, negatively charged E117 and D119 in red, and polar Q90, Q121 and N124 in purple. **D.** The estimated electrostatic potential is mapped to the surface of AvrSr50. **E** and **F**. The qualitative and quantitative cell death phenotypes on *Nicotiana benthamiana*. The optical density (OD_{600}) was set to 0.3 for receptors and effectors, respectively, and the receptors were expressed under pRPP13. Indicated receptor and effector pairs were co-infiltrated. The cell death phenotypes were recorded at three days post infiltration. **F**. The mode intensity of the infiltrated spots was measured with

298   imageJ across the given number of biological replicates in bold. The statistics were calculated with one-way ANOVA followed by
299   a post-hoc Tukey Honestly Significant Difference test. The compact letters indicate significant differences between groups. **G** and
300   **H**. The predicted poses of Sr50 and AvrSr50 in Model III and IV. Some parts of a loop between β2–β3, mostly including an
301   unstructured region, are removed from AvrSr50 for visualization (positions 42-66). **I** and **J**. The superposition of AvrSr50. The
302   entire complex structures of the two models were superposed to fix the coordinates of Sr50 consistent. The AvrSr50 structures are
303   then visualized. **K**. The local environment around Sr50's K711 in Model IV.

304   Although we had some confidence in Model III, we were uncertain whether ColabDock had not introduced any
305   unexpected alterations in the structures, such as backbone clashes in Model II (Fig. 4G). We used ColabFold to
306   eliminate abnormal structural features and remodel the flexible loop structures by providing Model III as a structural
307   template. This refined model, Model IV, was nearly identical to Model III, with only slight alterations in the
308   positioning of AvrSr50 relative to the LRR domain of Sr50 (Fig. 4H and 4J). In this model, the terminal alpha helix
309   of AvrSr50 enriched with positively charged side chains was positioned closely to Sr50's D643 and K711, although
310   AvrSr50's R128 was not oriented to form direct interaction with Sr50's D643 (Fig. 4K)

311   **Multiple Sr50^{K711D} double mutants enhance cell death against AvrSr50^{QCMJC}**

312   Unlike Model I (Fig. 1B), Model IV placed AvrSr50's Q121 near the terminal LRRs of Sr50—LRRs 13 and 14 in
313   particular (Fig. 5A). We decided to introduce additional mutations to Sr50^{K711D}, targeting W822, E847 and N849 on
314   these LRRs. These residues were mutated to negatively charged aspartic and glutamic acids, as well as polar
315   asparagine and glutamine, except for N849Q. Among tested double mutants, Sr50$^{K711D/W822N}$, Sr50$^{K711D/W822Q}$,
316   Sr50$^{K711D/E847D}$, Sr50$^{K711D/N849D}$ and Sr50$^{K711D/N849E}$ could induce HR against AvrSr50^{QCMJC} (Fig. 5B and 5C). The
317   average mode intensity of these double mutants was clearly greater than Sr50^{K711D} and AvrSr50^{QCMJC}, collectively
318   suggesting that based on our final structural model, we could successfully restore the recognition against the escape
319   mutant. Moreover, the recognition against AvrSr50 was not severely attenuated by these additional mutations (Fig.
320   5B and 5C).

321   **The Sr50 K711D mutation leads to synergistic impacts and is required for the engineered mutants to recognize**
322   **AvrSr50^{QCMJC}**

323   To gain more insights into the effect of the second layer of mutations introduced to Sr50^{K711D}, we created Sr50^{W822N},
324   Sr50^{W822Q}, Sr50^{E847D}, Sr50^{N849D} and Sr50^{N849E} single mutants and examined their abilities to induce HR against
325   AvrSr50 and AvrSr50^{QCMJC} (Fig. 5D and S9). Sr50^{W822N} and Sr50^{W822Q} single mutants led to detectable HR when co-
326   infiltrated with AvrSr50^{QCMJC} (Fig. 5E); however, a comparable level of autoactivity was induced, likely indicating
327   that the observed HR cannot be specifically associated with AvrSr50^{QCMJC} recognition. When the K711D mutation is
328   additionally introduced, the resulting Sr50$^{K711D/W822N}$ and Sr50$^{K711D/W822Q}$ double mutants were no longer autoactive,
329   while inducing stronger HR against AvrSr50^{QCMJC} (Fig. 5C). The E847D substitution led to the complete loss of the
330   receptor's ability to recognize AvrSr50 (Fig. 5D). Sr50^{N849D} and Sr50^{N849E} could still recognize AvrSr50 but did not
331   gain the ability to cause cell death against AvrSr50^{QCMJC}. In all these cases, the phenotypes of these single mutants
332   were altered when the K711D mutation was introduced, with gain of AvrSr50^{QCMJC} recognition and without losing
333   ability to interact with AvrSr50 (Fig. 5B).

334   The phenotypic discrepancy between the single mutants and the double mutants was unexpected, as we mostly
335   postulated that mutation effects are likely additive, if the two mutations happen distantly. To gain more insights into
336   the interplay between substitutions, we generated all combinations of single to triple mutants that include K711D,
337   W822N, E847D and N849E and quantified the magnitude of HR when the receptor was co-infiltrated with infiltration
338   buffer, AvrSr50 or AvrSr50^{QCMJC} (Fig. 5B, 5D, 5F and S9). Two triple mutants, Sr50$^{K711D/W822N/E847D}$ and

339 Sr50$^{K711D/W822N/N849E}$, could induce robust HR against AvrSr50^{QCMJC}. In particular, the magnitude of HR between
340 Sr50$^{K711D/W822N/E847D}$ and AvrSr50^{QCMJC} was comparable to Sr50 and AvrSr50, despite the recognition of AvrSr50
341 becoming weaker (Fig. 5C). Sr50$^{K711D/E847D/N849E}$ could not recognize AvrSr50^{QCMJC}, even though Sr50$^{K711D/N849E}$ and
342 Sr50$^{K711D/E847D}$ did, possibly suggesting that the two negatively charged side chains of E847D and N849E may be
343 interfering with each other, hindering the recognition. No other combinations of mutations could lead to robust gain
344 of AvrSr50^{QCMJC} recognition. All mutants that induced HR specifically towards AvrSr50^{QCMJC} required the K711D
345 substitution.
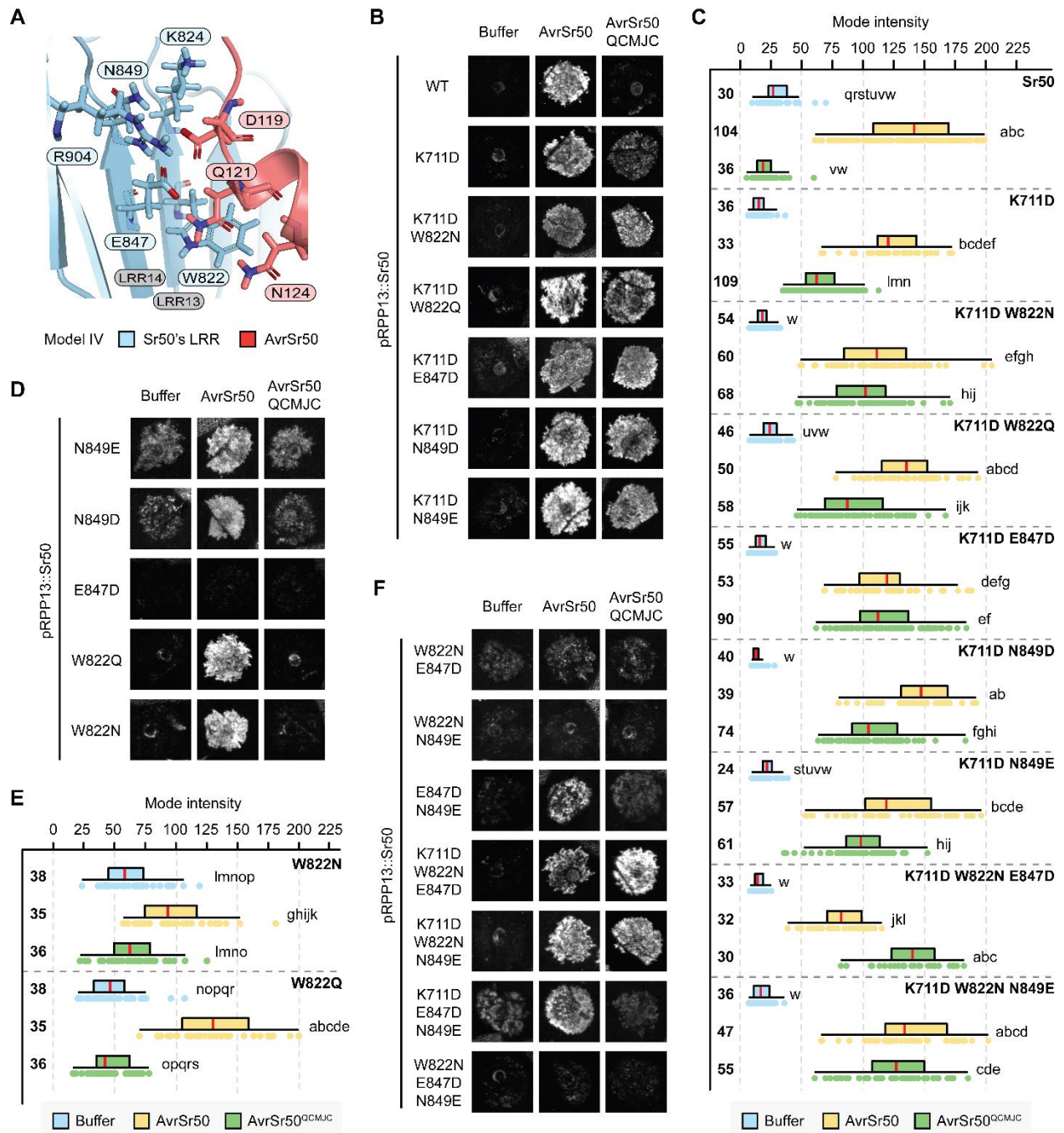
346
347 **Figure 5. Engineered double and triple Sr50 mutants induce robust HR against AvrSr50^{QCMJC}**

13

348 **A**. The local environment around AvrSr50's Q121 in Model IV. **B** to **F**. The qualitative and quantitative cell death phenotypes on
349 *Nicotiana benthamiana*. The optical density (OD$_{600}$) was set to 0.3 for receptors and effectors, respectively, and the receptors were
350 expressed under pRPP13. Indicated receptor and effector pairs were co-infiltrated. The cell death phenotypes were recorded at
351 three days post infiltration. **C** and **E**. The mode intensity of the infiltrated spots was measured with imageJ across the given number
352 of biological replicates in bold. The statistics were calculated with one-way ANOVA followed by a post-hoc Tukey Honestly
353 Significant Difference test. The compact letters indicate significant differences between groups.

354 **Engineered Sr50 alleles overlaps with a patch of hvLRRs is essential for effector binding, yet they are distinct**
355 **from natural variation**

356 We previously curated a set of 89 NLRs belonging to the MLA family sourced from Pooideae species (Tamborski et
357 al. 2023). Of these, 16 members were identified as part of the Sr50 homologous group based on their close
358 phylogenetic distances to Sr50. To characterize receptor residues involved in effector recognition, we quantified
359 sequence variations using normalized Shannon entropy and mapped these values onto the predicted Sr50 structure.
360 This revealed that a central effector binding site identified in our experiments is indeed associated with highly variable
361 LRR (hvLRR) residues (Prigozhin and Krasileva 2021; Tamborski et al. 2023). Notably, a patch of hvLRRs with the
362 greatest Shannon Entropy were distributed at the terminal LRRs above the central beta sheets (Fig. 6A) that includes
363 K824 and R904 shown as critical specificity-determinants. These regions also contained W822, E847 and N849, which
364 were altered to enhance the AvrSr50^{QCMJC} recognition.

365 Furthermore, in proximity to the hvLRR patch are three central tryptophan residues—W771, W799, and W822—
366 which we initially hypothesized to be essential for affinity towards AvrSr50 through hydrophobic interactions (Fig.
367 1C and 6A). We observed that W799, closest to the hvLRR patch, is essential for AvrSr50 recognition and cannot be
368 replaced by tyrosine or phenylalanine, while they can substitute W771 (Fig. S10). Our structural hypothesis suggests
369 that this hvLRR patch is crucial for interaction with the central binding site of AvrSr50, particularly involving residues
370 D119 and Q121, the mutations of which were shown to induce recognition escape (Fig. 2 and 3). This potentially
371 probes the rapid co-evolution at the interaction interface between the receptor and effector.
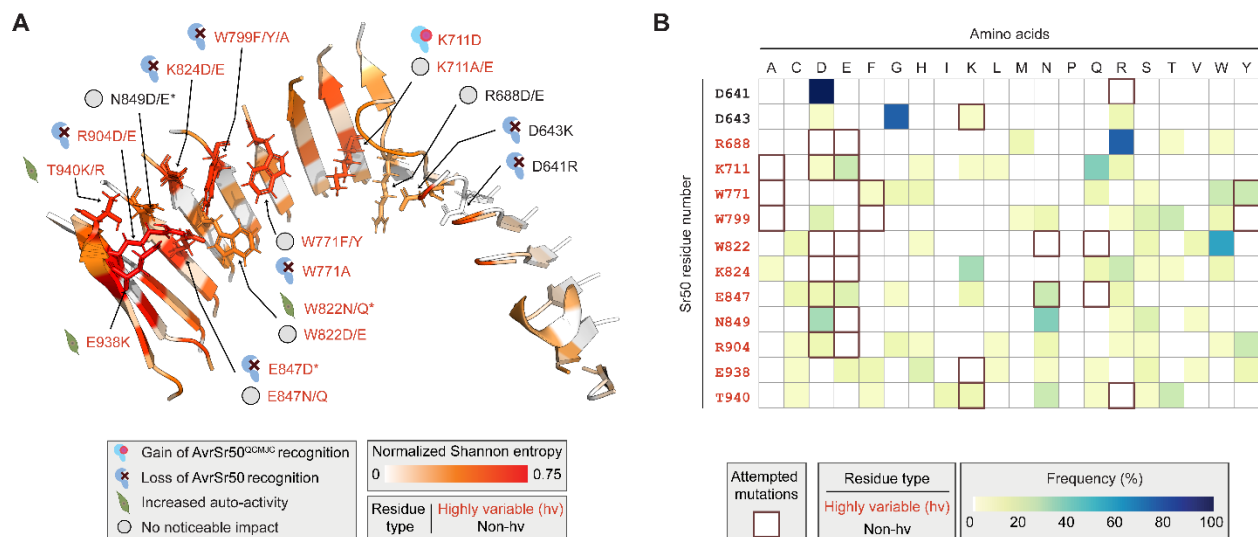
372
373 **Figure 6. The structural and evolutionary feature of mutagenized receptor residues**
374
375 **A**. Inner beta strands of leucine-rich repeat (LRR) domain of Sr50. The residue is colored based on normalized Shannon entropy
376 scores, which indicate variability of homologous sequences within the Sr50 family. The score ranges from 0 (no sequence
377 variability) to 1 (complete variability). The score was capped at 0.75 for visualization. The positions chosen for mutagenesis and

14

378 the phenotypes of single mutants are indicated. The mutations indicated with asterisks lead to different phenotypes when K711D
379 mutation is introduced together. **B**. The frequency of amino acids within the Sr50 family in the given homologous positions. The
380 mutations introduced in this study are colored brown.

382 In contrast, D641 and D643 were non-hvLRRs, with D641 displaying perfect sequence conservation among the
383 homologous sequences and glycine being the predominant amino acid at position 643 (Fig. 7B). This conservation
384 may be attributed to their proximity to the NB-ARC domain, where incompatible mutations might also disrupt
385 interdomain interactions.

386 Within the 16 members of the Sr50 homologous group, the mutations we introduced to create functional Sr50 double
387 and triple mutants occurred rarely (Fig. 7B). Aspartic acid appeared in 6.25% of instances at position 711, asparagine
388 and glutamine in no instances at position 822, aspartic acid in 12.5% at position 847, and glutamic acid in no instances
389 at position 849. Aspartic acid was relatively frequent at position 849 with 30% of instances. No homologous
390 sequences, however, had the combinations of amino acids shown to induce HR against AvrSr50^{QCMJC}. Collectively,
391 although our structure-guided rational design approaches targeted the region of the receptor in which the greatest
392 natural variation occurs, our engineered receptor alleles were distinct from known natural variations (Fig. 5 and 6B).

393 **Amino acid substitutions in input sequences alter the behavior of AlphaFold 2, and the K711D substitution**
394 **enables prediction of the complex structure of Sr50 and AvrSr50**

395 We initially observed that AF2-Multimer was unable to accurately predict the structure of Sr50 and AvrSr50
396 complexes (Fig. 7A and S1). We attempted modeling the complex structure of Sr50$^{K711D/W822N/E847D}$ and AvrSr50^{QCMJC},
397 as the engineered receptor mutant could induce strong HR against the effector. Although AF2 assigned low accuracy
398 to the prediction (Fig. 7B), AF2 predicted a complex structure of Sr50$^{K711D/W822N/E847D}$ and AvrSr50^{QCMJC} that nearly
399 matched model IV (Fig. 7A). Interestingly, the predicted heterodimeric complex of Sr50$^{K711D/W822N/E847D}$ and AvrSr50
400 also showed great similarity.

401 To examine the sequence variation that switched the behavior of AF2, we modeled the protein complex structure of
402 Sr50^{K711D}, Sr50^{W822N} and Sr50^{E847D} with AvrSr50. Only the K711D substitution, but not W822N and E847
403 substitutions, could alter the outcome of AF2, enabling the prediction of the Sr50^{K711D} and AvrSr50 complex that
404 agreed with Model IV (Fig. 7A and S11). This observation was consistent for Sr50^{K711D} and AvrSr50^{QCMJC} (Fig.7A).
405 These results collectively indicated that the single amino substitution, K711D, not only altered the biological response
406 of the receptor to the effector (Fig. 1) but was also sufficient to change the outcome of AF2 prediction.

407 In a recent study, Gómez De La Cruz et al. modeled the structure of AvrSr50 and Sr50^{3BI} with AF2 to predict the
408 potential binding site of AvrSr50 (2024). Sr50^{3BI} contains a scratch of 25 amino acids at positions 920 to 950
409 transferred from barley NLR MLA3 that recognizes its effector Pwl2. Although Sr50 and Sr50^{3BI} differ only by 12
410 amino acids, AF2 could produce a high confidence model for Sr50^{3BI} and AvrSr50. Under the identical conditions
411 used to predict Sr50^{K711D} and AvrSr50, we modeled the complex structure of Sr50^{3BI} and AvrSr50 and could obtain
412 the heterodimeric complex structure as previously reported (Gómez De La Cruz et al. 2024) (Fig. 7A). This model
413 showed good agreement with Model IV as well as the AF models of Sr50^{K711D} and Sr50$^{K711D/W822N/E847D}$ complexes
414 (Fig. 7A and 7C). However, AF2 failed to predict the structure of Sr50^{3BI} and AvrSr50^{QCMJC} (Fig. 7A). Notably, the
415 predicted accuracy of the complex structure (iptm) and the predicted aligned errors showed high confidence for Sr50^{3BI}
416 and AvrSr50, as reported by the authors (Gómez De La Cruz et al. 2024). Despite similar topologies, AF2 did not
417 report comparable confidence for Sr50^{K711D} or Sr50$^{K711D/W822N/E847D}$ and AvrSr50 or AvrSr50^{QCMJC} (Fig. 7B). These
418 results indicated that slight changes in the input sequences can alter the behavior and outcome of AF2 prediction; This

419 potentially suggests that iterative in silico mutagenesis of input sequences could aid the prediction of NLR-effector
420 complexes.
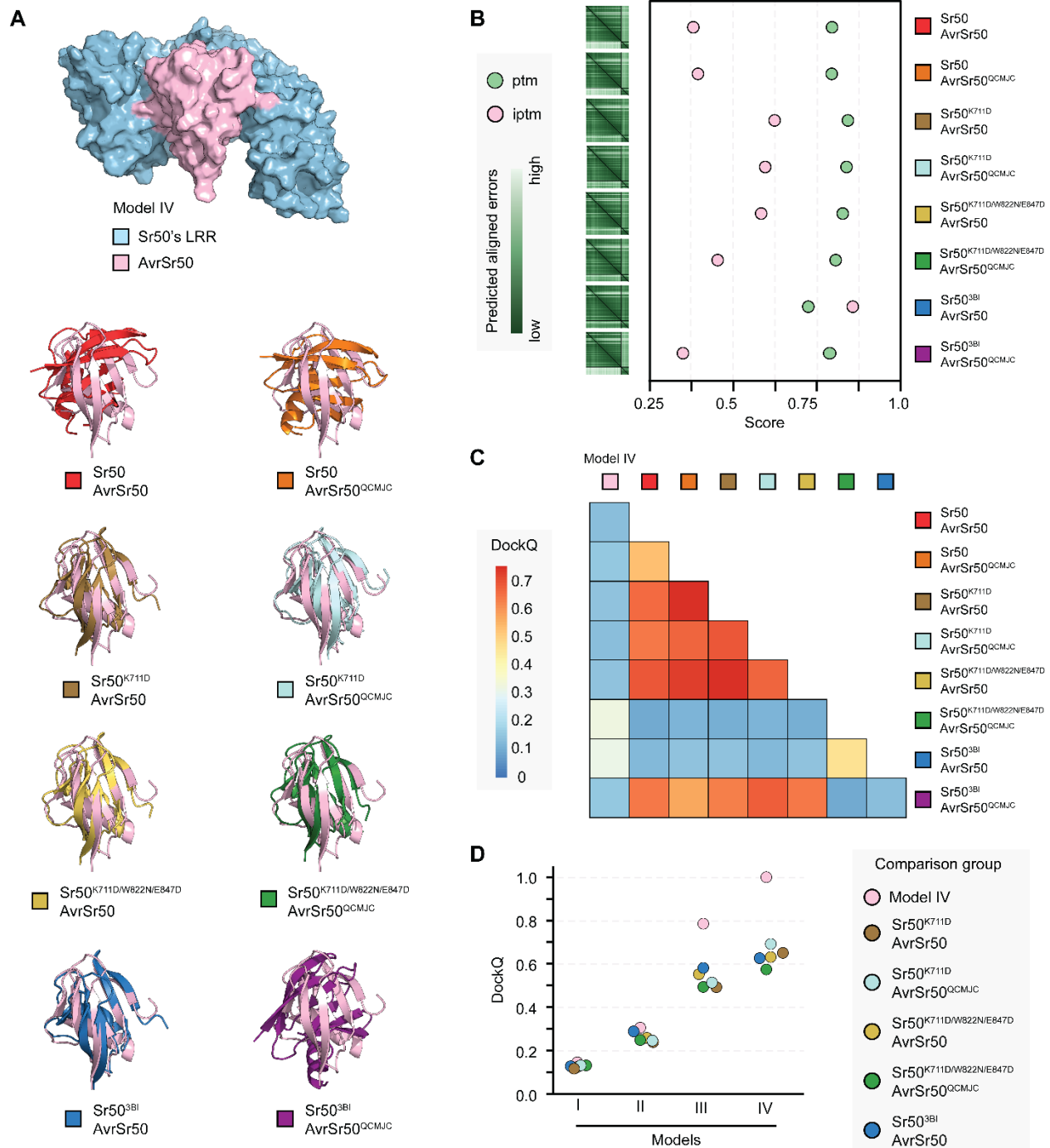
421
422 **Figure 7. AlphaFold 2 predicts the complex structure of Sr50 and AvrSr50**

423 **A.** The structural superposition of AvrSr50 in AlphaFold 2 (AF2) models compared to Model IV. The predicted protein complex
424 structures were superposed against Model IV to keep the coordinates of Sr50 consistent. The AvrSr50 structures were then
425 visualized. **B**. The confidence scores of AF2 models. The ptm and iptm scores, as well as the predicted aligned error (PAE) plots

426 are shown for the best model (Elfmann and Stülke 2023). The colored boxes correspond to the predicted model specified in A. **C**.
427 The comparison of protein complex structures with DockQ scores. The DockQ scores can be divided into incorrect (0 < DockQ <
428 0.23), acceptable quality (0.23 ≤ DockQ < 0.49), medium quality (0.49 ≤ DockQ < 0.80) and high quality (0.80 ≤ DockQ ≤ 1). The
429 heterodimeric complexes of Sr35 and AvrSr50 solved by two different groups using the Cryo-EM structures produce a DockQ
430 score of 0.76 (PDB: 7XC2 and 7XE0) (Förderer et al. 2022; Zhao et al. 2022). The DockQ score was capped at 0.76 for comparison.
431 The loop between β2–β3, mostly including an unstructured region, is excluded (positions 42-66). **D**. The comparison of structural
432 hypotheses to Model IV and AF structures.

Discussion

434 Experimentally determined NLR-effector complex structures can aid in developing engineering strategies against
435 evolving effectors, but they may not always guarantee success. These structures provide static snapshots, while
436 proteins are inherently dynamic. Predicting the impact of new effector mutations on the interaction with NLRs and
437 host disease phenotypes remains challenging even with reliable structures. Therefore, accumulating evolutionary and
438 experimental data is crucial for effective engineering solutions. Our results highlight that iterative computational
439 modeling approaches together with experimental determination of structural constraints is an effective strategy for
440 engineering the plant intracellular immune receptor to restore recognition of the escape effector mutants. Below, we
441 outline main lessons and suggestions from our work that could be used for guiding experimental resurrection of other
442 NLRs as well as for developing machine learning models.

Reducing search space for efficient and rational mutagenesis-based approaches

444 Our approach operates without experimentally determined receptor-effector complex structures and evolutionary data
445 from receptors known to recognize their escape effector mutants. In this circumstance, exploring all mutational
446 landscapes through experiments is currently impossible due to high order of information complexity. To bypass this
447 problem, we simplify candidate residue selection and mutagenesis process, relying on the central biochemical
448 principle of protein-protein interactions: while hydrophobic interactions provide the main energy for ligand binding,
449 it is the charged residues that determine ligand specificity through ionic or hydrogen bonds. Our experiments
450 demonstrated that altering the specificity determinants to amino acids with their opposite charges can be a practical
451 approach to confirm the interactions between receptor and effector residues and their proximity.

452 A recent study demonstrated that the single L902S substitution led to gain of recognition of Avr_{A13}-1 in MLA7
453 (Lawson et al. 2024). Similar solutions may exist for Sr50 to acquire resistance to $AvrSr50^{QCMJC}$, but identifying them
454 through our methodology can be challenging. In similar contexts, if the effector mutants escape through steric clashes
455 and changes in affinity-determinants, engineering solutions would be more difficult to obtain. Nevertheless, our work
456 effectively elucidates mutation effects on the NLR-effector interactions across the LRR domain, creates engineering
457 solutions and generates structural hypotheses, which can be useful to solve current and future problems against
458 evolving effectors.

All models are wrong, but some are useful

460 Our workflow to predict NLR-effector interactions showed that, as of today, modeling-based engineering approaches
461 need to be iterative. We used three iterations of experimentally constrained modeling and a round of computational
462 refinement to derive the final solution, Model IV. Although the actual accuracy of the model can only be evaluated
463 when Cryo-EM structure becomes available, this model showed great similarity to independently derived AF models
464 (Fig. 7). When we compared all modeling iterations to Model IV and other AF models to evaluate their accuracy, we
465 noted that our initial structural hypothesis (Model I) was completely incorrect with the DockQ scores between 0.11

466 and 0.15 (Fig. 7D). However, in each iteration of model refinement, the structural hypothesis continued to improve,
467 suggesting that although these models were imperfect, they were useful to derive the next hypothesis.

468 The main aim of our structural hypotheses is to refine and streamline the extensive and random screening processes
469 into more targeted approaches by providing structural contexts and hypotheses. This approach does not aim to
470 precisely depict molecular interactions or replace experimentally determined structures but to offer practical solutions
471 in the absence of experimentally determined or accurately predicted NLR-effector complex structures. This
472 methodology can be expanded to other NLR-effector systems, providing a useful framework for addressing evolving
473 effector challenges.

Hacking AlphaFold

475 Our study initially began with the observation that AF struggles to predict the correct topology of receptor-effector
476 complexes, as evidenced by the recent Cryo-EM structure of MLA13 and its effector AVR_{A13}-1 (Lawson et al. 2024).
477 Surprisingly, AF2 produced high-confidence models for MLA3 and its effector Pwl2, as well as for $Sr50^{3BI}$ and
478 AvrSr50 (Gómez De La Cruz et al. 2024). Moreover, a single amino acid change in Sr50 rectified the previously
479 unsuccessful prediction of Sr50 and AvrSr50 complexes, resulting in models that match our final structural hypothesis
480 (Fig. 7). AF2 is not specifically trained to predict the impact of small amino acid mutations in protein folding.
481 However, our study, along with the previous research, suggests that small changes in input sequences can significantly
482 alter the outcome of the complex structure prediction. This observation hints at the potential for in silico screening of
483 receptor-effector complexes, provided we can uncover methods to effectively 'hack' AF2 to our advantage.
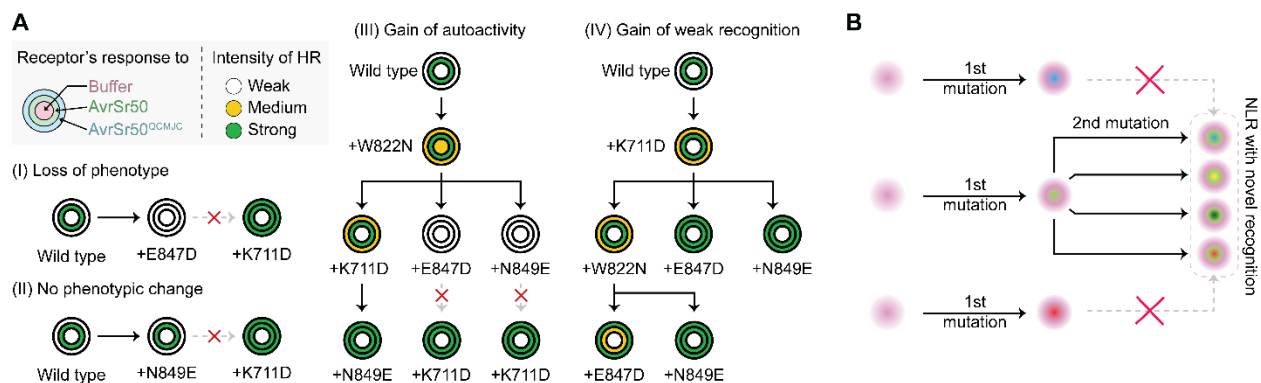
Figure 8. The initial mutation significantly influences subsequent evolutionary opportunities

A. Phenotypes of engineered Sr50 mutants along possible mutational paths. The circles are composed of three layers, which indicate the strength of hypersensitive responses (HR) of the given receptors towards buffer (autoactivity), AvrSr50 and $AvrSr50^{QCMJC}$ co-infiltrations. Each wild type Sr50 accumulates a single mutation per event. The paths highlight additional mutations towards enhanced HR against $AvrSr50^{QCMJC}$ or reduced autoactivity. **B.** The impact of the initial mutations in subsequent mutational opportunities. The initial mutation can significantly influence subsequent evolutionary opportunities, either limiting or expanding them, even though the overall paths may lead to an identical set of mutations.

The order of mutations impacts the emergence of functional NLRs against escape effector mutants

493 The order of mutations and resulting phenotypic changes provide insights into the natural evolution of functional
494 NLRs (Fig. 8). Consider a scenario where wheat accumulates mutations in the interaction with *P. graminis* QCMJC
495 in the field. Substitutions like E847D, which abolish the interaction with effectors, or N849E, which do not lead to

496 phenotypic changes, may appear first (Fig. 8A; I and II). Individuals with these mutations would likely be selected
497 against, preventing them from acquiring a second mutation, such as K711D, even though the double mutations can
498 ensure resistance against AvrSr50^{QCMJC}. To resurrect resistance through multiple mutations, NLRs would initially
499 need to develop weak to intermediate resistance, as seen in Sr50^{K711D}, or some level of autoactivity at the cost of
500 development, as observed in Sr50^{W822N} (Fig. 8A; III and IV). These early mutations could lead to additional mutations
501 that either enhance HR or reduce autoactivity in regulatory regions or protein-coding sequences. Notably, the
502 emergence of K711D as an initial mutation opens more avenues for acquiring robust resistance compared to other
503 tested mutations (Fig. 8A). This suggests that multiple solutions exist to achieve gain of recognition towards escape
504 mutants, but the path to these solutions may be restricted (Fig. 8B). In other words, the initial mutation can significantly
505 influence subsequent evolutionary opportunities, either preventing or expanding them, even though the overall paths
506 may lead to an identical set of final mutations.

507 We postulate that Sr50's K711 only had a supplementary role in the initial interactions between Sr50 and AvrSr50.
508 The mutations at position 711 did not significantly impact the AvrSr50 recognition (Fig. 1 and S5). However, when
509 K121 of AvrSr50^{QCMJC} disrupts the interaction with the hvLRRs patch around Sr50's K824 and R904 (Fig. 3 and Fig.
510 6), the K711D substitution in Sr50 would likely facilitates additional interactions with the alpha helix of AvrSr50^{QCMJC}
511 enriched with positively charged arginines (Fig. 4). This interaction may be subtle as the HR between Sr50^{K711D} and
512 AvrSr50^{QCMJC} was only weak to intermediate (Fig. 1 and 2); however, this may be essential for the upper alpha helix
513 of AvrSr50^{QCMJC} to align properly with the terminal LRRs of Sr50. This alignment potentially allows for more stable
514 binding to the receptor, thereby enabling the engineered receptor mutants to recognize the escape mutant only in the
515 presence of the K711D substitution (Fig. 5).

516 **Expanding to other NLR-effector systems**

517 Our data, derived from 6,000 quantifications from infiltrations, provides robust representation of a wide spectrum of
518 biological responses between cognate NLR and effector variants (Table S1). This dataset can be useful in correlating
519 biological responses and in silico prediction, serving as an experimentally derived training dataset for the future
520 computational or machine learning approaches. Expanding recognition specificity to other paralogs and sequence-
521 unrelated structurally similar (SUSS) effectors is the next challenge (Seong and Krasileva 2021, 2023). While AvrSr50
522 forms a SUSS effector family, no other members are yet known to interact with NLRs. Alternatively, MLA receptors
523 from barley and their cognate effectors from powdery mildew, *Blumeria graminis*, can be more compelling systems
524 (Saur et al. 2019). Not only do MLAs share close evolutionary relationships with Sr50 (Tamborski et al. 2023), but
525 also they recognize sequence-divergent or SUSS effectors originating from an extensively expanded RNAse-like
526 protein family with many experimentally determined structures (Pennington et al. 2019; Cao et al. 2023; Seong and
527 Krasileva 2023; Lawson et al. 2024). Leveraging preexisting rich experimental data can aid in inferring initial
528 structural hypotheses and predicting the molecular interactions between MLAs and their effectors. Elucidating the
529 complex structures of diverse Sr and MLA receptors and their effectors can reveal how plants evolved NLRs to detect
530 SUSS effectors, and through the framework of this study, we may guide experimental designs and engineering
531 solutions for other NLR-effector systems.

532 # Methods

533 **Vectors and mutagenesis**

534 We used the previously generated constructs (Tamborski et al. 2023). The receptor constructs carried *Sr50* under the
535 *pRPP13* promoter and the *tNos* terminator, or the *p35S* promoter and the *t35S* terminator. The effector constructs
536 contained *AvrSr50* and *AvrSr50^{QCMJC}* with the *p35S* promoter and *t35S* terminator. All additional mutations were

537 introduced with QuikChange Lightning Site-directed Mutagenesis Kits from Agilent. We followed the standard
538 protocol but reduced the volume of all reagents by four. All primers and mutants used in this study are available in
539 Table S2.
540

541 **Transformation and mutation confirmation**

542 XL10-Gold ultracompetent cells were transformed, following the standard protocol given in QuikChange Lightning
543 Site-directed Mutagenesis Kits. Plasmids were extracted from a liquid culture inoculated with a single colony,
544 following the standard protocol of The QIAprep Spin Miniprep Kit. The desired mutation was confirmed with Sanger
545 sequencing.
546

547 About 40 μL of *Agrobacterium tumefaciens* GV3101:pMP90 was mixed with 100 ng of the mutagenized plasmid in
548 a 1.5 ml plastic tube and transferred to an electroporation cuvette. After an electric pulse, the cells were transferred
549 back to the tube with 250 μL of LB media and shaken at 28°C and 250 rpm for two hours. The liquid culture was
550 plated on LB agar containing Carbenicillin, Rifampicin and Gentamicin, and the plates were incubated at 28°C for
551 two days. A single colony was picked and transferred to a liquid LB medium and grown for a day.
552

553 We additionally confirmed the mutations in the transformed *Agrobacterium*. Each mutant was replated from its
554 glycerol stock on LB agar containing Carbenicillin, Rifampicin and Gentamicin and grown at 28°C for two days.
555 Colonies were scraped from the plates, resuspended in 10 μL of water and incubated at 98°C for 10 minutes. The cells
556 were centrifuged for one minute, and target regions with introduced mutations were amplified, following the PCR
557 Protocol for Phusion® High-Fidelity DNA Polymerase (M0530) or for repliQa HiFi ToughMix. The mutation was
558 confirmed with Sanger sequencing.
559

560 *Agrobacterium*-mediated transient gene expression in *N. benthamiana*

561 The liquid cultures containing *Agrobacterium* transformants were centrifuged at 6,400g for five minutes, and the
562 pellets were resuspended in infiltration medium composed of deionized water, 10 mM MES (pH 5.6), 10 mM $MgCl_2$,
563 150 μM acetosyringone. The optical density (OD_{600}) of each transformant was re-adjusted to 0.6. The transformants
564 carrying receptors and effectors were mixed to adjust the OD_{600} of the receptors to 0.1 (for p35S) or 0.3 (for *pRPP13*).
565 The OD_{600} of the effectors was set to 0.3. *N. benthamiana*'s 4-5 weeks old leaves were inoculated with the suspension
566 using blunt syringes. The phenotypes were recorded at 2 dpi for the *p35S* promoter and at 3 dpi for the *pRPP13*
567 promoter.
568

569 **Cell death quantification and statistics**

570 The infiltrated *N. benthamiana* leaves were imaged with the ChemiDoc MP Imaging System and Image Lab v5.2.1
571 (https://www.bio-rad.com). Following the previous publication (Landeo Villanueva et al. 2021), we used green epi-
572 illumination with a filter set to 605/50. Exposure time was set to 0.5 seconds. To quantify the cell death, we manually
573 selected the treated area and measured the mode of intensity with ImageJ v2.14.0 (Rueden et al. 2017). The statistics
574 were computed in R v4.1.3 (Ihaka and Gentleman 1996). One-way ANOVA was performed to compare significant
575 differences between the sample means, and post-hoc Tukey's honest significance test was followed for pairwise
576 comparisons.
577

578 **Protein extraction and co-immunoprecipitation assays**

579 Six *N. benthamiana* leaf discs of 0.8 cm in diameter were collected at 1 dpi after *Agrobacterium*-mediated infiltrations.
580 The samples were frozen in liquid nitrogen and ground with a bead beater at 1,500 Hz for 1 min with two 3.2 mm
581 stainless beads. Protein was extracted with 300 μL of the 2x Laemmli sample buffer (Biorad) with 5% β-
582 mercaptoethanol. Samples were boiled at 95°C for 5 min and centrifuged at maximum speed for 10 min at 4 °C.

583 Supernatants were transferred into fresh tubes for SDS PAGE analysis. 10L of protein extraction was separated on
584 15% Mini-PROTEAN® TGX™ Precast Protein Gels (Biorad, 15-well), transferred to PVDF membrane (Biorad) at
585 300 mA for 70 min. Immunoblotting was performed using rat HRP-conjugated α-HA (monoclonal 3F10, Roche) and
586 subsequently chemiluminescent substrate SuperSignal™ West Pico PLUS (Thermo Scientific™). Total protein was
587 stained using Ponceau S.
588
589 **Protein structure prediction and visualization**

590 The initial Sr50 and AvrSr50 structures were predicted by AlphaFold v2.2.2 (Jumper et al. 2021), with the full
591 database, available homologous templates and model_preset set to monomer. Protein complexes were predicted with
592 ColabFold v1.5.2 that relies on AlphaFold v2.3.1, with alphafold2_multimer_v3 and template_model set to pdb100,
593 as well as AlphaFold 3 (Evans et al. 2021; Mirdita et al. 2022; Abramson et al. 2024). We used customized ColabDock
594 (Feng et al. 2023) through Google Colab to obtain Models II and III. Pairwise constraints derived from the experiments
595 were provided. Among the five models produced by ColabDock, the best structure (1st_best) was used for the
596 analyses. The side chains of this structure were relaxed with Amber, a module within ColabFold.
597
598 The AF2 models, which were compared to Model IV, were generated with ColabFold v1.5.5. The structure of
599 AvrSr50^{QCMJC} was submitted as a template (PDB:7MQQ) (Ortiz et al. 2022). All loop regions were excluded from the
600 initial PDB file to allow ColabFold to remodel the flexible loop structures. Five models were predicted with the
601 alphafold2_multimer_v3 model, and the best structure was relaxed. The default parameters were used, except for
602 num_recycles set to 24 and pair_mode changed to unpaired. We used PyMOL v2.5.2 for protein structure
603 superposition and visualization (The PyMOL Molecular Graphics System). The analysis of the electrostatic potential
604 relied on the APBS plugin in PyMOL (Jurrus et al. 2018).
605
606 **Molecular docking and initial model selection**

607 The best Sr50 and AvrSr50 monomer models were submitted to ZDOCK, HDOCK and ClusPro web servers as a
608 receptor and a ligand, respectively (Pierce et al. 2014; Kozakov et al. 2017; Yan et al. 2020). From each server, 100
609 models were obtained, and each model was evaluated for the following criteria, based on the backbone distances ($C_β$
610 or $C_α$ of glycine). First, all Sr50 residues in the coiled-coil and NB-ARC domains (positions 1 to 520) are not within
611 8 Å of AvrSr50. Second, AvrSr50 should touch the NB-ARC latch–a loop structure exposed from the NB-ARC
612 domain–, forming close contact with LRRs (positions 492-499). Specifically, Sr50's E494 is within 12 Å of AvrSr50.
613 This residue was chosen as the predicted Sr50 structure suggested that its sidechain points toward the putative effector
614 binding site surrounded by the concave of LRR units. The distance cut-off was relaxed based on our assumption that
615 the interaction between the NB-ARC latch and the effectors occur through long side chains. Third, AvrSr50's Q121
616 is within 8 Å of Sr50's LRR domain (Ortiz et al. 2022; Tamborski et al. 2023). Fourth, at least 12 hvLRR residues on
617 the inner β-strands or upper loops of Sr50 are within 8 Å of AvrSr50 (Prigozhin and Krasileva 2021). Then, the effector
618 poses of the models that satisfied these criteria were clustered with the RMSD (root mean square deviation) cut-off of
619 3.0. We required at least two predictors to produce similar poses, despite their differing scoring functions and
620 underlying algorithms. A representative conformation was chosen from each cluster based on the model ranking.
621
622 **Protein structure prediction and visualization**

623 The initial Sr50 and AvrSr50 structures were predicted by AlphaFold v2.2.2 (Jumper et al. 2021), with the full
624 database, available homologous templates and model_preset set to monomer. Protein complexes were predicted with
625 ColabFold v1.5.2 that relies on AlphaFold v2.3.1, with alphafold2_multimer_v3 and template_model set to pdb100,
626 as well as AlphaFold 3 (Evans et al. 2021; Mirdita et al. 2022; Abramson et al. 2024)..We used customized ColabDock
627 (Feng et al. 2023) through Google Colab. Among the five models produced by ColabDock, the best structure that
628 satisfied all provided restraints was selected. To further refine this model, we ran AlphaFold through ColabFold with
629 the model given as a customized template. The best prediction was relaxed with amber.

630   The AF2 models, which were compared to Model IV, were generated with ColabFold v1.5.5. The structure of
631   AvrSr50^{QCMJC} was submitted as a template (PDB:7MQQ) (Ortiz et al. 2022). All loop regions were excluded from the
632   initial PDB file to allow ColabFold to remodel the flexible loop structures. Five models were predicted with the
633   alphafold2_multimer_v3 model, and the best structure was relaxed. The default parameters were used, except for
634   num_recycles set to 24 and pair_mode changed to unpaired. We used PyMOL v2.5.2 for protein structure
635   superposition and visualization. The analysis of the electrostatic potential relied on the APBS plugin in PyMOL (Jurrus
636   et al. 2018). Structural similarities between complex structures were quantified with DockQ v2.1.1 (Basu and Wallner
637   2016).

Evolutionary analyses

640   The multiple sequence alignment of MLA family members and the normalized Shannon entropy for the Sr50
641   homologous group were obtained from the previous study and analyzed with the identical workflow (Tamborski et al.
642   2023).

Data availability

645   All scripts and command lines used for computational analyses are available and recorded in Github:
646   https://github.com/s-kyungyong/Sr50_AvrSr50/. All input, intermediate and output data were deposited in Zenodo:
647   https://zenodo.org/doi/10.5281/zenodo.13205869

Acknowledgements

Contributions

657   K.S. conceptualized and designed the project. K.S. wrote the manuscript with edits from K.V.K and W.W. W.W.
658   performed Western blot. K.S. performed computational analyses. K.S., W.W., B.V., A.D., G.R., R.K. and L.P.
659   conducted experiments. K.V.K. supervised the research.

Competing interests

662   The authors declare no competing interests.

References

666   **Abramson J, Adler J, Dunger J, Evans R, Green T, Pritzel A, Ronneberger O, Willmore L, Ballard AJ,**
667   **Bambrick J, et al.** Accurate structure prediction of biomolecular interactions with AlphaFold 3. Nature.
668   2024. https://doi.org/10.1038/s41586-024-07487-w
669   **Arora S, Steuernagel B, Gaurav K, Chandramohan S, Long Y, Matny O, Johnson R, Enk J, Periyannan S,**
670   **Singh N, et al.** Resistance gene cloning from a wild crop relative by sequence capture and association
671   genetics. Nat Biotechnol. 2019:**37**(2):139–143. https://doi.org/10.1038/s41587-018-0007-9
672   **Baggs E, Dagdas G, and Krasileva K**. NLR diversity, helpers and integrated domains: making sense of the NLR
673   IDentity. Curr Opin Plant Biol. 2017:**38**:59–67. https://doi.org/10.1016/j.pbi.2017.04.012
674   **Basu S and Wallner B**. DockQ: A Quality Measure for Protein-Protein Docking Models. PLOS ONE.
675   2016:**11**(8):e0161879. https://doi.org/10.1371/journal.pone.0161879
676   **Bentham AR, De La Concepcion JC, Benjumea JV, Kourelis J, Jones S, Mendel M, Stubbs J, Stevenson CEM,**

677 **Maidment JHR, Youles M, et al.** Allelic compatibility in plant immune receptors facilitates engineering of
678 new effector recognition specificities. Plant Cell. 2023:**35**(10):3809–3827.
679 https://doi.org/10.1093/plcell/koad204
680 **Cao Y, Kümmel F, Logemann E, Gebauer JM, Lawson AW, Yu D, Uthoff M, Keller B, Jirschitzka J, Baumann
681 U, et al.** Structural polymorphisms within a common powdery mildew effector scaffold as a driver of
682 coevolution with cereal immune receptors. Proc Natl Acad Sci. 2023:**120**(32):e2307604120.
683 https://doi.org/10.1073/pnas.2307604120
684 **Cesari S, Xi Y, Declerck N, Chalvon V, Mammri L, Pugnière M, Henriquet C, De Guillen K, Chochois V,
685 Padilla A, et al.** New recognition specificity in a plant immune receptor by molecular engineering of its
686 integrated domain. Nat Commun. 2022:**13**(1):1524. https://doi.org/10.1038/s41467-022-29196-6
687 **Chen J, Upadhyaya NM, Ortiz D, Sperschneider J, Li F, Bouton C, Breen S, Dong C, Xu B, Zhang X, et al.**
688 Loss of *AvrSr50* by somatic exchange in stem rust leads to virulence for *Sr50* resistance in wheat. Science.
689 2017:**358**(6370):1607–1610. https://doi.org/10.1126/science.aao4810
690 **Contreras MP, Pai H, Selvaraj M, Toghani A, Lawson DM, Tumtas Y, Duggan C, Yuen ELH, Stevenson CEM,
691 Harant A, et al.** Resurrection of plant disease resistance proteins via helper NLR bioengineering. Sci Adv.
692 2023:**9**(18):eadg3861. https://doi.org/10.1126/sciadv.adg3861
693 **Dangl JL, Horvath DM, and Staskawicz BJ**. Pivoting the Plant Immune System from Dissection to Deployment.
694 Science. 2013:**341**(6147):746–751. https://doi.org/10.1126/science.1236011
695 **De La Concepcion JC, Franceschetti M, MacLean D, Terauchi R, Kamoun S, and Banfield MJ**. Protein
696 engineering expands the effector recognition profile of a rice NLR immune receptor. eLife. 2019:**8**:e47713.
697 https://doi.org/10.7554/eLife.47713
698 **Dodds PN and Rathjen JP**. Plant immunity: towards an integrated view of plant–pathogen interactions. Nat Rev
699 Genet. 2010:**11**(8):539–548. https://doi.org/10.1038/nrg2812
700 **Elfmann C and Stülke J**. PAE viewer: a webserver for the interactive visualization of the predicted aligned error for
701 multimer structure predictions and crosslinks. Nucleic Acids Res. 2023:**51**(W1):W404–W410.
702 https://doi.org/10.1093/nar/gkad350
703 **Evans R, O'Neill M, Pritzel A, Antropova N, Senior A, Green T, Žídek A, Bates R, Blackwell S, Yim J, et al.**
704 Protein complex prediction with AlphaFold-Multimer (Bioinformatics).
705 https://doi.org/10.1101/2021.10.04.463034
706 **Farnham G and Baulcombe DC**. Artificial evolution extends the spectrum of viruses that are targeted by a disease-
707 resistance gene from potato. Proc Natl Acad Sci. 2006:**103**(49):18828–18833.
708 https://doi.org/10.1073/pnas.0605777103
709 **Feng S, Chen Z, Zhang C, Xie Y, Ovchinnikov S, Gao Y, and Liu S**. ColabDock: inverting AlphaFold structure
710 prediction model for protein-protein docking with experimental restraints (Bioinformatics).
711 https://doi.org/10.1101/2023.07.04.547599
712 **Förderer A, Li E, Lawson AW, Deng Y, Sun Y, Logemann E, Zhang X, Wen J, Han Z, Chang J, et al.** A wheat
713 resistosome defines common principles of immune receptor channels. Nature. 2022:**610**(7932):532–539.
714 https://doi.org/10.1038/s41586-022-05231-w
715 **Gómez De La Cruz D, Zdrzałek R, Banfield MJ, Talbot NJ, and Moscou MJ**. Molecular mimicry of a pathogen
716 virulence target by a plant immune receptor. 2024. https://doi.org/10.1101/2024.07.26.605320
717 **Harris CJ, Slootweg EJ, Goverse A, and Baulcombe DC**. Stepwise artificial evolution of a plant disease resistance
718 gene. Proc Natl Acad Sci. 2013:**110**(52):21189–21194. https://doi.org/10.1073/pnas.1311134110
719 **Huang H, Huang S, Li J, Wang H, Zhao Y, Feng M, Dai J, Wang T, Zhu M, and Tao X**. Stepwise artificial
720 evolution of an Sw-5b immune receptor extends its resistance spectrum against resistance-breaking isolates
721 of *Tomato spotted wilt virus*. Plant Biotechnol J. 2021:**19**(11):2164–2176. https://doi.org/10.1111/pbi.13641
722 **Ihaka R and Gentleman R**. R: A Language for Data Analysis and Graphics. J Comput Graph Stat. 1996:**5**(3):299–
723 314. https://doi.org/10.1080/10618600.1996.10474713
724 **Jones JDG and Dangl JL**. The plant immune system. Nature. 2006:**444**(7117):323–329.
725 https://doi.org/10.1038/nature05286
726 **Jumper J, Evans R, Pritzel A, Green T, Figurnov M, Ronneberger O, Tunyasuvunakool K, Bates R, Žídek A,
727 Potapenko A, et al.** Highly accurate protein structure prediction with AlphaFold. Nature.
728 2021:**596**(7873):583–589. https://doi.org/10.1038/s41586-021-03819-2
729 **Jurrus E, Engel D, Star K, Monson K, Brandi J, Felberg LE, Brookes DH, Wilson L, Chen J, Liles K, et al.**
730 Improvements to the APBS biomolecular solvation software suite. Protein Sci. 2018:**27**(1):112–128.
731 https://doi.org/10.1002/pro.3280
732 **Kourelis J, Schuster M, Demir F, Mattinson O, Krauter S, Kahlon PS, O'Grady R, Royston S, Bravo-Cazar**

AL, Mooney BC, et al. Bioengineering secreted proteases converts divergent Rcr3 orthologs and paralogs into extracellular immune co-receptors. Plant Cell. 2024:koae183. https://doi.org/10.1093/plcell/koae183

Kozakov D, Hall DR, Xia B, Porter KA, Padhorny D, Yueh C, Beglov D, and Vajda S. The ClusPro web server for protein–protein docking. Nat Protoc. 2017:**12**(2):255–278. https://doi.org/10.1038/nprot.2016.169

Kroj T, Chanclud E, Michel-Romiti C, Grand X, and Morel J. Integration of decoy domains derived from protein targets of pathogen effectors into plant immune receptors is widespread. New Phytol. 2016:**210**(2):618–626. https://doi.org/10.1111/nph.13869

Landeo Villanueva S, Malvestiti MC, Van Ieperen W, Joosten MHAJ, and Van Kan JAL. Red light imaging for programmed cell death visualization and quantification in plant–pathogen interactions. Mol Plant Pathol. 2021:**22**(3):361–372. https://doi.org/10.1111/mpp.13027

Lawson AW, Flores-Ibarra A, Cao Y, An C, Neumann U, Gunkel M, Saur IML, Chai J, Behrmann E, and Schulze-Lefert P. The barley MLA13-AVR $_{A13}$ heterodimer reveals principles for immunoreceptor recognition of RNase-like powdery mildew effectors. 2024. https://doi.org/10.1101/2024.07.14.603419

Liu F, Yang Z, Wang C, Martin R, Qiao W, Carette JE, Luan S, Nogales E, and Staskawicz B. The activated plant NRC4 immune receptor forms a hexameric resistosome (Plant Biology). https://doi.org/10.1101/2023.12.18.571367

Ma S, Lapin D, Liu L, Sun Y, Song W, Zhang X, Logemann E, Yu D, Wang J, Jirschitzka J, et al. Direct pathogen-induced assembly of an NLR immune receptor complex to form a holoenzyme. Science. 2020:**370**(6521):eabe3069. https://doi.org/10.1126/science.abe3069

Madhuprakash J, Toghani A, Contreras MP, Posbeyikian A, Richardson J, Kourelis J, Bozkurt TO, Webster M, and Kamoun S. A disease resistance protein triggers oligomerization of its NLR helper into a hexameric resistosome to mediate innate immunity. 2024. https://doi.org/10.1101/2024.06.18.599586

Mago R, Zhang P, Vautrin S, Šimková H, Bansal U, Luo M-C, Rouse M, Karaoglu H, Periyannan S, Kolmer J, et al. The wheat Sr50 gene reveals rich diversity at a cereal disease resistance locus. Nat Plants. 2015:**1**(12):15186. https://doi.org/10.1038/nplants.2015.186

Maidment JH, Shimizu M, Bentham AR, Vera S, Franceschetti M, Longya A, Stevenson CE, De La Concepcion JC, Białas A, Kamoun S, et al. Effector target-guided engineering of an integrated domain expands the disease resistance profile of a rice NLR immune receptor. eLife. 2023:**12**:e81123. https://doi.org/10.7554/eLife.81123

Martin R, Qi T, Zhang H, Liu F, King M, Toth C, Nogales E, and Staskawicz BJ. Structure of the activated ROQ1 resistosome directly recognizing the pathogen effector XopQ. Science. 2020:**370**(6521):eabd9993. https://doi.org/10.1126/science.abd9993

Mirdita M, Schütze K, Moriwaki Y, Heo L, Ovchinnikov S, and Steinegger M. ColabFold: making protein folding accessible to all. Nat Methods. 2022:**19**(6):679–682. https://doi.org/10.1038/s41592-022-01488-1

Möller M and Stukenbrock EH. Evolution and genome architecture in fungal plant pathogens. Nat Rev Microbiol. 2017:**15**(12):756–771. https://doi.org/10.1038/nrmicro.2017.76

Ortiz D, Chen J, Outram MA, Saur IML, Upadhyaya NM, Mago R, Ericsson DJ, Cesari S, Chen C, Williams SJ, et al. The stem rust effector protein AvrSr50 escapes Sr50 recognition by a substitution in a single surface-exposed residue. New Phytol. 2022:**234**(2):592–606. https://doi.org/10.1111/nph.18011

Pennington HG, Jones R, Kwon S, Bonciani G, Thieron H, Chandler T, Luong P, Morgan SN, Przydacz M, Bozkurt T, et al. The fungal ribonuclease-like effector protein CSEP0064/BEC1054 represses plant immunity and interferes with degradation of host ribosomal RNA. PLOS Pathog. 2019:**15**(3):e1007620. https://doi.org/10.1371/journal.ppat.1007620

Pierce BG, Wiehe K, Hwang H, Kim B-H, Vreven T, and Weng Z. ZDOCK server: interactive docking prediction of protein–protein complexes and symmetric multimers. Bioinformatics. 2014:**30**(12):1771–1773. https://doi.org/10.1093/bioinformatics/btu097

Prigozhin DM and Krasileva KV. Analysis of intraspecies diversity reveals a subset of highly variable plant immune receptors and predicts their binding sites. Plant Cell. 2021:**33**(4):998–1015. https://doi.org/10.1093/plcell/koab013

Rueden CT, Schindelin J, Hiner MC, DeZonia BE, Walter AE, Arena ET, and Eliceiri KW. ImageJ2: ImageJ for the next generation of scientific image data. BMC Bioinformatics. 2017:**18**(1):529. https://doi.org/10.1186/s12859-017-1934-z

Sánchez-Vallet A, Fouché S, Fudal I, Hartmann FE, Soyer JL, Tellier A, and Croll D. The Genome Biology of Effector Gene Evolution in Filamentous Plant Pathogens. Annu Rev Phytopathol. 2018:**56**(1):21–40. https://doi.org/10.1146/annurev-phyto-080516-035303

Sarris PF, Cevik V, Dagdas G, Jones JDG, and Krasileva KV. Comparative analysis of plant immune receptor

architectures uncovers host proteins likely targeted by pathogens. BMC Biol. 2016:**14**(1):8. https://doi.org/10.1186/s12915-016-0228-7

Saur IM, Bauer S, Kracher B, Lu X, Franzeskakis L, Müller MC, Sabelleck B, Kümmel F, Panstruga R, Maekawa T, et al. Multiple pairs of allelic MLA immune receptor-powdery mildew AVRA effectors argue for a direct recognition mechanism. eLife. 2019:**8**:e44471. https://doi.org/10.7554/eLife.44471

Segretin ME, Pais M, Franceschetti M, Chaparro-Garcia A, Bos JIB, Banfield MJ, and Kamoun S. Single Amino Acid Mutations in the Potato Immune Receptor R3a Expand Response to *Phytophthora* Effectors. Mol Plant-Microbe Interactions®. 2014:**27**(7):624–637. https://doi.org/10.1094/MPMI-02-14-0040-R

Selvaraj M, Toghani A, Pai H, Sugihara Y, Kourelis J, Yuen ELH, Ibrahim T, Zhao H, Xie R, Maqbool A, et al. Activation of plant immunity through conversion of a helper NLR homodimer into a resistosome (Plant Biology). https://doi.org/10.1101/2023.12.17.572070

Seong K and Krasileva KV. Computational Structural Genomics Unravels Common Folds and Novel Families in the Secretome of Fungal Phytopathogen *Magnaporthe oryzae*. Mol Plant-Microbe Interactions®. 2021:**34**(11):1267–1280. https://doi.org/10.1094/MPMI-03-21-0071-R

Seong K and Krasileva KV. Prediction of effector protein structures from fungal phytopathogens enables evolutionary analyses. Nat Microbiol. 2023:**8**(1):174–187. https://doi.org/10.1038/s41564-022-01287-6

Tamborski J and Krasileva KV. Evolution of Plant NLRs: From Natural History to Precise Modifications. Annu Rev Plant Biol. 2020:**71**(1):355–378. https://doi.org/10.1146/annurev-arplant-081519-035901

Tamborski J, Seong K, Liu F, Staskawicz BJ, and Krasileva KV. Altering Specificity and Autoactivity of Plant Immune Receptors Sr33 and Sr50 Via a Rational Engineering Approach. Mol Plant-Microbe Interactions®. 2023:**36**(7):434–446. https://doi.org/10.1094/MPMI-07-22-0154-R

The PyMOL Molecular Graphics System.

Wang J, Hu M, Wang J, Qi J, Han Z, Wang G, Qi Y, Wang H-W, Zhou J-M, and Chai J. Reconstitution and structure of a plant NLR resistosome conferring immunity. Science. 2019a:**364**(6435):eaav5870. https://doi.org/10.1126/science.aav5870

Wang J, Wang J, Hu M, Wu S, Qi J, Wang G, Han Z, Qi Y, Gao N, Wang H-W, et al. Ligand-triggered allosteric ADP release primes a plant NLR complex. Science. 2019b:**364**(6435):eaav5868. https://doi.org/10.1126/science.aav5868

Yan Y, Tao H, He J, and Huang S-Y. The HDOCK server for integrated protein–protein docking. Nat Protoc. 2020:**15**(5):1829–1852. https://doi.org/10.1038/s41596-020-0312-x

Zdrzałek R, Stone C, De La Concepcion JC, Banfield MJ, and Bentham AR. Pathways to engineering plant intracellular NLR immune receptors. Curr Opin Plant Biol. 2023:**74**:102380. https://doi.org/10.1016/j.pbi.2023.102380

Zhao Y-B, Liu M-X, Chen T-T, Ma X, Li Z-K, Zheng Z, Zheng S-R, Chen L, Li Y-Z, Tang L-R, et al. Pathogen effector AvrSr35 triggers Sr35 resistosome assembly via a direct recognition mechanism. Sci Adv. 2022:**8**(36):eabq5108. https://doi.org/10.1126/sciadv.abq5108